

Chapter 4. Experimental set-up for wind tunnel tests

This chapter describes the boundary layer wind tunnel at the Ruhr-University Bochum, the model of the Solar Updraft Tower and an outline of the tests. Moreover, the preliminary results on the circular cylinder (without rings) are presented. Issues like the influence of the Reynolds number and the choice of surface roughness are also addressed in this chapter.

4.1 WiSt wind tunnel (Ruhr-University Bochum)

4.1.1 Geometry of the boundary layer wind tunnel

WiSt laboratory at Ruhr-University Bochum (Windingenieurwesen und Strömungsmechanik <http://www.ruhr-uni-bochum.de/wist>) is an open circuit wind tunnel with a total length of about 17 m. The tunnel itself has a length of 9.3 m. The test section is 1.8 m in width and 1.6 m in height. In case of need, the upper ceiling of the tunnel can be raised until 1.9 m. A turntable in the test section allows to test different wind directions, if necessary. A honeycomb grid is located at the inlet of the tunnel.



Figure 4.1 WiSt boundary layer wind tunnel at Ruhr-University Bochum

The turbulent boundary layer develops over a length of about 7.6 m. After a castellated barrier having a maximum height of 425 mm, there are three turbulent generators of 1.5 m in height. They are built according to Counihan's specifications (Counihan, 1969), as reported in the following sketch (Figure 4.2). The roughness field consists of six panels with $36 \times 36 \times 36 \text{ mm}^3$ cubes alternated to $36 \times 36 \times 18 \text{ mm}^3$ square prisms. It creates the lowest and most important part of the boundary layer, which undergoes a natural evolution along the wind tunnel and the largest eddy reaches approximately the

thickness of this surface layer, i.e. 30-40 cm. The turbulence in the upper layer is created by turbulence generators. At a distance of about 3.5 times the height of the turbulent generators, the two layers merge and continue to grow together. The castellated barrier acts as an adjustment element. All these facilities (castellated barrier, turbulence generators and roughness field) are removed in case of low-turbulence tests in empty tunnel and approximately uniform flow. The boundary layer at each wall affects a distance of about 30 cm.

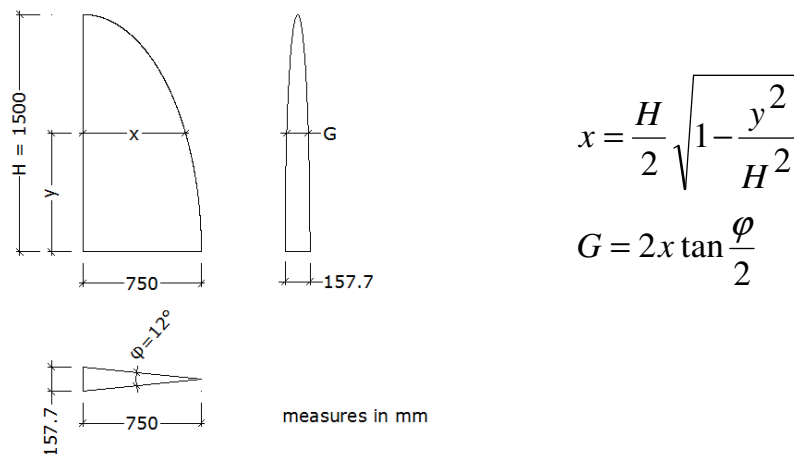


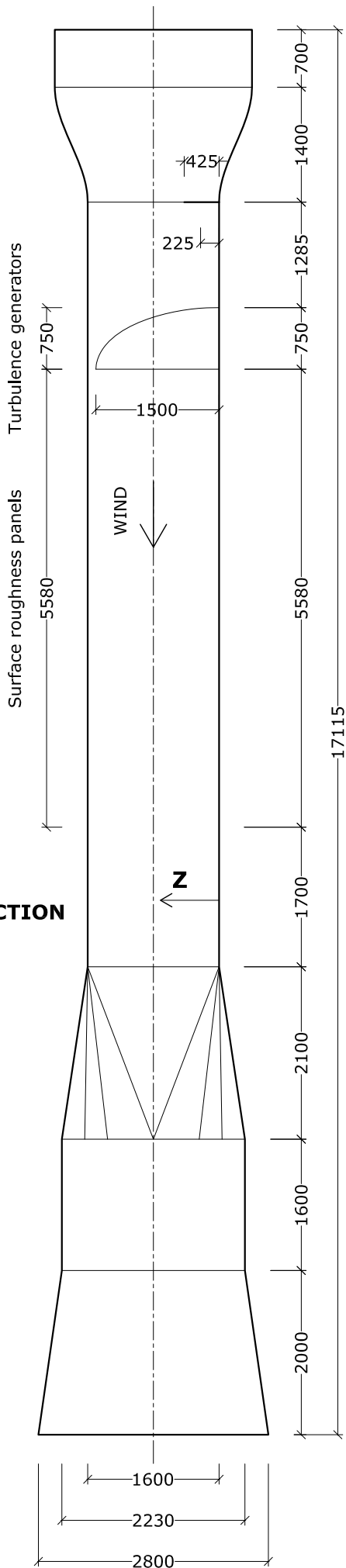
Figure 4.2 Turbulent generators of Couihhan type

The diffuser and the centrifugal fan are placed at the end of the wind tunnel. The engine allows to attain a maximum wind speed of about 28-30 m/s with 1500 turns per minute of the fan. A Prandtl tube allows to measure the dynamic pressure of the incoming flow. Temperature sensors acquire temperature during the measurements. It allows to calculate the air density and therefore the mean wind speed by applying Bernoulli equation. The Prandtl tube is normally placed at 1.3 m in height – out of the influence of the wall of the wind tunnel – but its position may change depending on the tests.

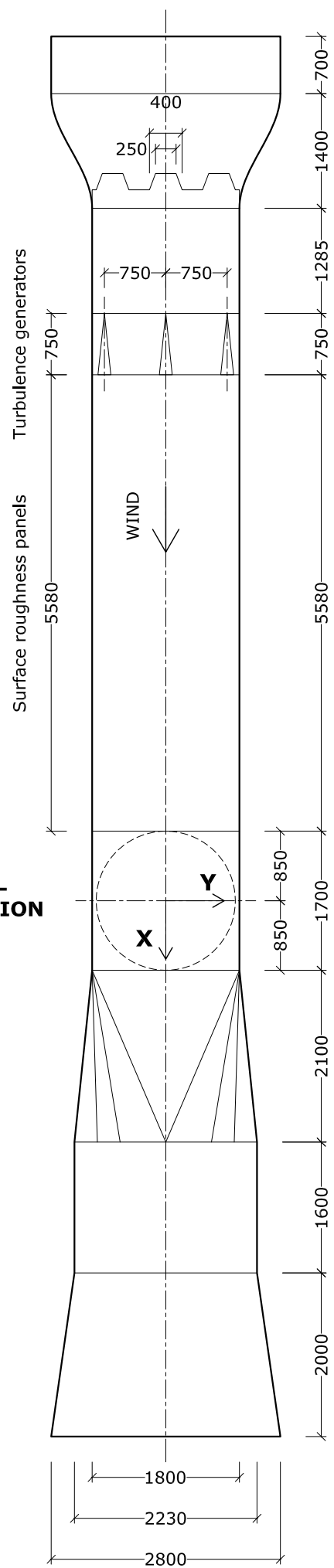


Figure 4.3 View of the model in the wind tunnel with turbulent facilities

**VERTICAL
CROSS-SECTION**



**HORIZONTAL
CROSS-SECTION**



4.1.2 Flow characteristics

The castellated barrier, the turbulent generators and the roughness field, previously described, produce a certain boundary layer namely RAU8. For the wind tunnel tests on the solar tower, however, a slightly modified version of RAU8 is adopted, due to the presence of the collector. It is named RAU8+collector (Figure 4.1). The collector, i.e. a smooth panel of 4 m in length, centered at the tower position, was introduced with the aim of creating a two-phase profile, as it should be expected in full-scale. Due to the presence of the collector, the last roughness panel (the shortest one, 0.33 m in length) had to be removed. The final set-up of the wind tunnel resulted like that:

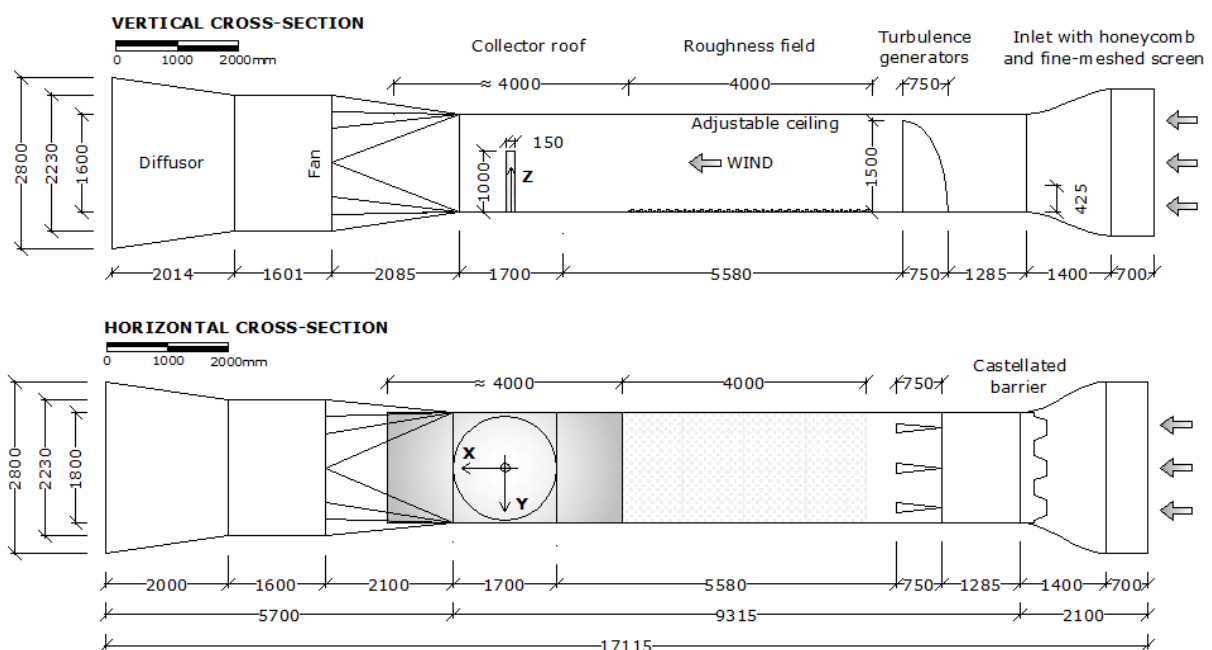


Figure 4.4 View of the Solar Tower in the wind tunnel at the Ruhr-University Bochum

The ESDU Data Items 82026 allow to estimate the height of the internal layer which develops after a roughness change, as that produced by the smooth collector roof. $z_{0,1}$ and $z_{0,2}$ are the roughness lengths corresponding to the upwind and downwind conditions, respectively. U_{z1} and U_{z2} are the resulting wind profiles. At a certain distance x from the step change in roughness, it can be assumed that the wind speed profile consists of a lower portion (internal layer), where the velocity is dependent on x and it is given by $K_x U_{z2}$, and an upper portion where the profile is the same as upwind. The height of the internal layer, at which the two portions intersect, can be estimated according to the ESDU procedure. If it is assumed that the smooth collector has a surface roughness $z_{0,2} = 0.005$ m, while the upwind conditions are those described in chapter 2 for the H&D model ($U_{z1}(10\text{m}) = 25$ m/s, $z_{0,1} = 0.05$ m, latitude = 23°), an internal layer of approximately 200 m can be calculated in the full-scale condition at a distance equal to the radius of the collector R_{coll} (Table 4.1).

Table 4.1 Effect of a step change in roughness according to ESDU 82026 at the tower position

Upwind conditions (full-scale)			Downwind conditions (full-scale)		
z_{01}	0.05	m	z_{02}	0.005	m
u_{*1}	1.898	m/s	u_{*2}	1.638	m/s
Internal layer height in m (full-scale)			h_i	201	
K _x factor at $x = R_{coll} = 2000$ m after the roughness change			0.9070		

Instruments for velocity measurements

The velocity profile is measured with hot-wires anemometers. Cross wires allow to measure two wind components (either u and v , or u and w). More than one probe can record simultaneously in the wind tunnel; the Multichannel CTA 54N80 by Dantec is an amplifier which allows to measure up to 16 channels. In the experiments, however, only two cross-wire probes were used (four channels) plus temperature and Prandtl velocity (two other channels). The A/D converter is the same as for pressure measurements (see section 4.1.3) and it is set to a sampling frequency of 2 kHz.

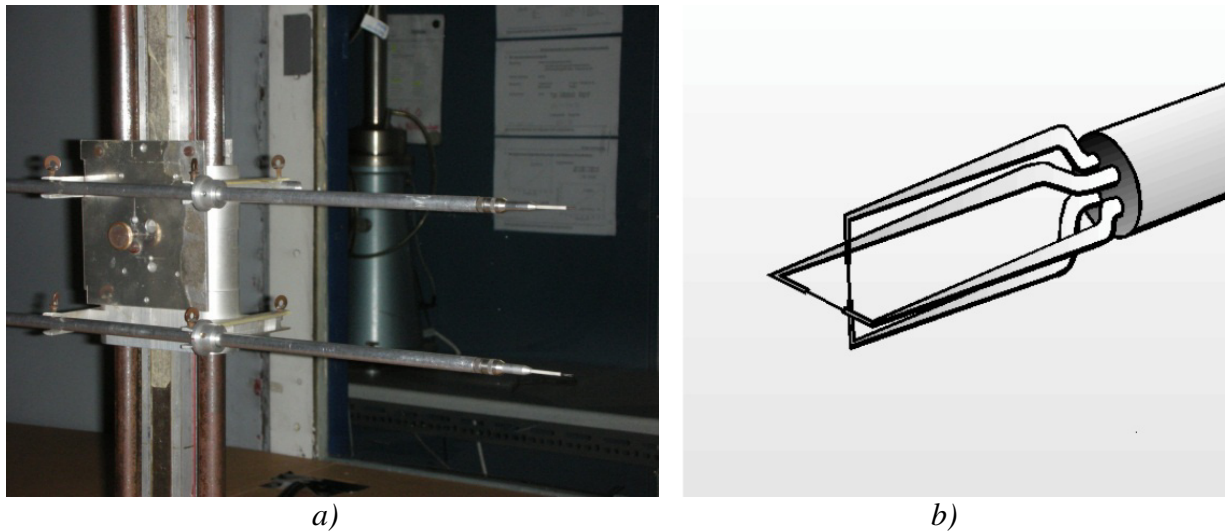


Figure 4.5 Miniature wires (X-array): a) during experiments; b) zoom

The multichannel CTA is designed for use with miniature wire probes (type 55P61-64) in combination with 4m probe cables. Each channel of the CTA can be set to a certain “decade resistance”, defined as twenty times the operating resistance. The latter depends on the resistances of the sensor, of the probe support and of the probe cable. The wires are 5 μm in diameter and 1.2 mm long. They are suspended between two needle-shaped prongs. The frequency bandwidth is 10 kHz and filters can be applied.

The anemometers are calibrated in laminar flow in the calibration tunnel. The calibration establishes a relation between the CTA output (voltages) and the flow velocity. It is performed by exposing the probe to a set of known velocities, U , and the corresponding voltages E are recorded. A fitting curve through the points (E,U) represents the transfer function to be used when converting data records from voltages into velocities. The fitting curve which is adopted is a polynomial curve of 4th order (equation (4.1)). The coefficients are calculated by fitting the data in the least-squares sense. An example reported is in Figure 4.6.

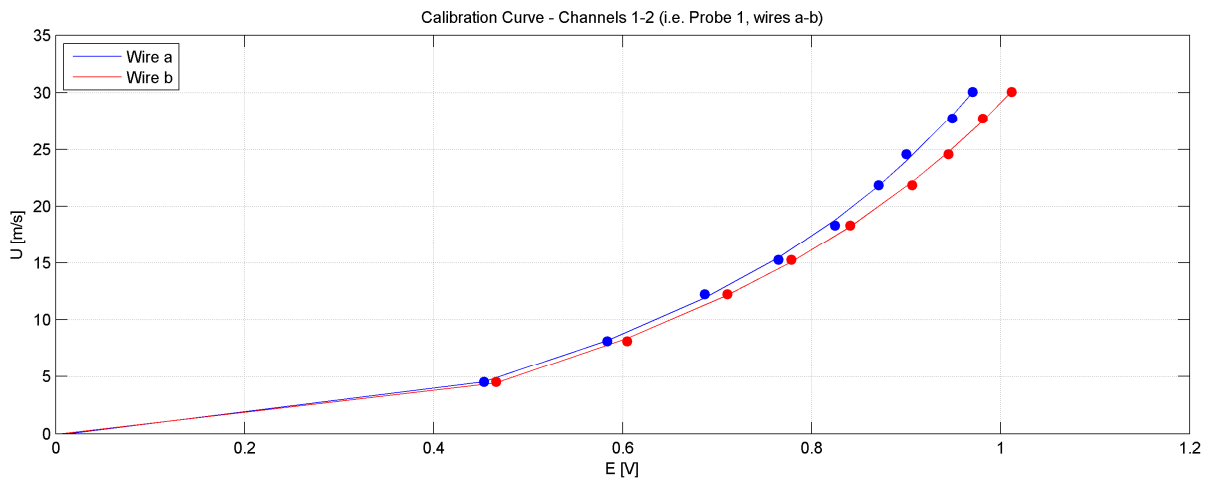


Figure 4.6 Calibration curve – wires a and b of one probe (experiment 24.10.2011)

$$U = C_0 + C_1 E + C_2 E^2 + C_3 E^3 + C_4 E^4 \quad (4.1)$$

If the temperature varies during calibration and the experiment, the recorded voltages must be corrected (E_{corr}) with the formula:

$$E_{corr} = \left(\frac{T_w - T_0}{T_w - T_a} \right)^{0.5} E_a \quad (4.2)$$

where: E_a = acquired voltage; T_w = sensor hot temperature = 250°; T_0 = ambient reference temperature (during calibration); T_a = ambient temperature during acquisition. The expression can be used for moderate temperature changes in air ($\pm 5^\circ\text{C}$). The useful range may be expanded (Jørgensen Finn E., 2002) by reducing the exponent from 0.5 to 0.4 or 0.3.

This formula is suggested by the practical guide of Dantec, but it was checked by measurements at several different temperatures before being applied in the experiments.

Results of velocity measurements

Mean wind profile, turbulence intensity, integral length scales and spectra are evaluated by hot-wires anemometers measurements. The mean wind profile is defined by using a power law according to formula (4.3).

$$\frac{U_m(z)}{U_{ref}} = \left(\frac{z}{z_{ref}} \right)^\alpha \quad (4.3)$$

The reference velocity is the velocity of the Prandtl tube U_{pra} . Unfortunately, during the tests, the mean level of the velocity measured by one of the two anemometers shifted to lower values. It is probably due to a sensible modification of the calibration curve. The mean values of that anemometer could not be used. Instead, the fluctuations did not result to be affected. The results of the available data for the mean wind profile are reported in Figure 4.7 and confirmed that the influence of the collector extends up to $z = 200$ mm. This fits very well the ESDU recommendation mentioned before (Table 4.1).

The turbulence intensity of the u-component is calculated according to the definition (4.4). The same applies to the components in the other directions, by using either σ_v or σ_w .

$$I_u(z) = \frac{\sigma_u(z)}{U_m(z)} \quad (4.4)$$

The integral length scales of turbulence represent an average size of the vortices associated to longitudinal, transversal and vertical turbulence in the x, y and z directions, respectively. Nine integral scales of turbulence can be defined: L_{ux} , L_{uy} , L_{uz} , L_{vx} , L_{vy} , L_{vz} , L_{wx} , L_{wy} , L_{wz} . They are calculated by integration from zero to infinite of the zero-lag covariance functions divided by the variance, i.e. the cross-correlation coefficients. For example, for the u-component they are:

$$L_{ux} = \frac{1}{\sigma_u^2} \int_0^{+\infty} R_u(\Delta x, 0) d\Delta x = \int_0^{+\infty} \rho_u(\Delta x, 0) d\Delta x \quad (4.5)$$

$$L_{uy} = \frac{1}{\sigma_u^2} \int_0^{+\infty} R_u(\Delta y, 0) d\Delta y = \int_0^{+\infty} \rho_u(\Delta y, 0) d\Delta y \quad (4.6)$$

$$L_{uz} = \frac{1}{\sigma_u^2} \int_0^{+\infty} R_u(\Delta z, 0) d\Delta z = \int_0^{+\infty} \rho_u(\Delta z, 0) d\Delta z \quad (4.7)$$

The integral length scale L_{ux} can be easily calculated by Taylor's hypothesis, which allows to use only one signal measured in one position, by assuming that the vortices move in the along-wind direction at the mean wind speed:

$$L_{ux} = U T_{ux} \quad (4.8)$$

T_{ux} is the integral time scale, i.e. the integral of the auto-correlation function from zero until infinite (equation (4.9)). In practical terms, the integration can be extended until the first zero crossing, because all the following undulations of the auto-correlation coefficient approximately average to zero. Also other methods exist, for example the exponential method, which assumes that the auto-correlation function has an exponential decay (Schrader, 1993). Alternately, T_{ux} can also be calculated by fitting the spectrum of the signal with an analytical expression of the velocity spectrum (e.g. von Karman spectrum in isotropic flow).

$$T_{ux} = \int_0^{\infty} \rho_{ux}(\tau) d\tau \quad (4.9)$$

Besides L_{ux} , for the purpose of this work it is especially important to investigate the integral length scale of the u-component in the z direction, i.e. L_{uz} . Approximately, in the atmospheric boundary layer flow, it is one half of L_{ux} , apart from very close to the ground. In this work, L_{uz} is calculated at each height by integration of the cross-correlation coefficients from zero until infinite (equation (4.10)). This requires simultaneous measurements of wind velocity in at least two points (Figure 4.5).

$$L_{u_z}(z_{ref}, \Delta z) = \int_0^{\infty} \rho_u(z_{ref}, \Delta z) d\Delta z \quad (4.10)$$

Vertical cross-correlations of the u-component in the undisturbed flow are measured both upwards and downwards at the following reference heights: 100-300-500-700-900-1100 mm. They are fitted with a negative exponential function, from which L_{uz} is easily derived:

$$\rho_u(\Delta z) = e^{-\frac{\Delta z}{L_{uz}}} \quad (4.11)$$

The spectra of the u and v components are reported in Figure 4.11 and Figure 4.12. In particular, the investigation of the cross-wind component (v) of the wind velocity is important for a deeper study of pressure fluctuations at the flanges of the cylinder and for transversal oscillations of the structure in a dynamic calculation. The spectrum of the v-component, compared to the spectrum of the u-component, appears to be shifted (Figure 4.13). It implies higher energy in the cross-wind direction at relatively high frequency, i.e. in the frequency range of most of structures sensitive to wind.

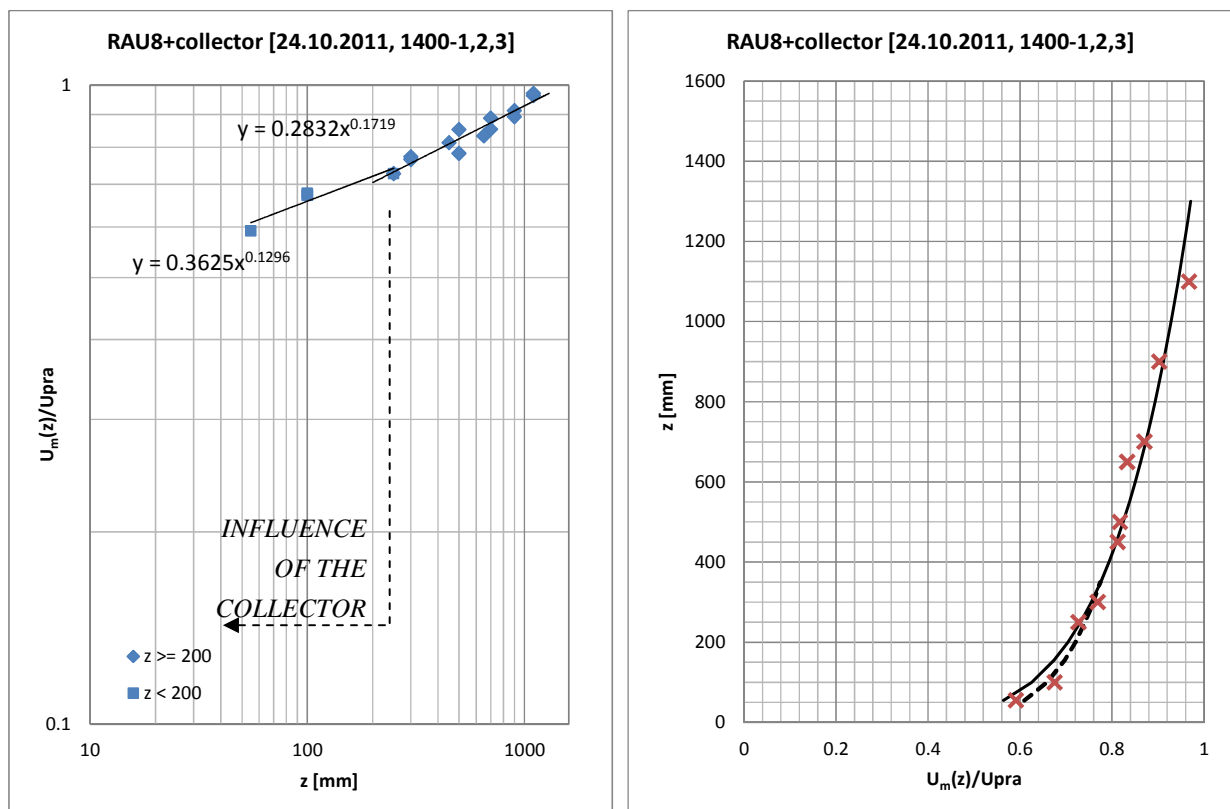


Figure 4.7 Mean wind profile (RAU8+collector)

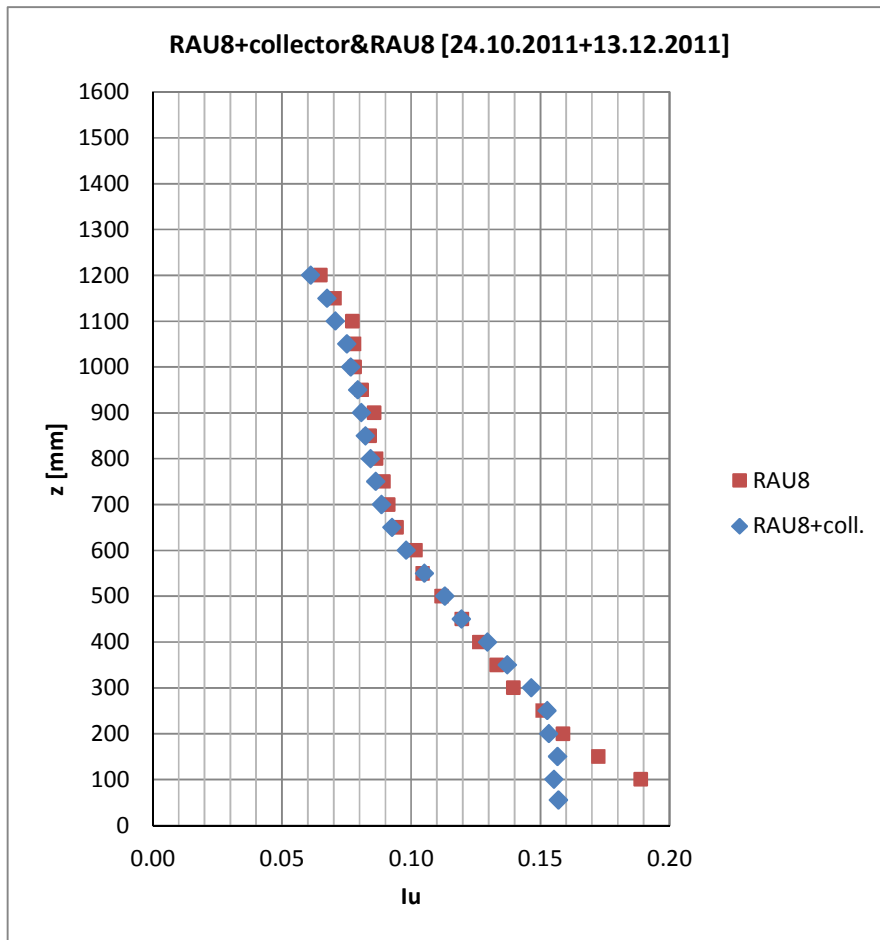


Figure 4.8 Turbulence intensity (RAU8+collector and RAU8)

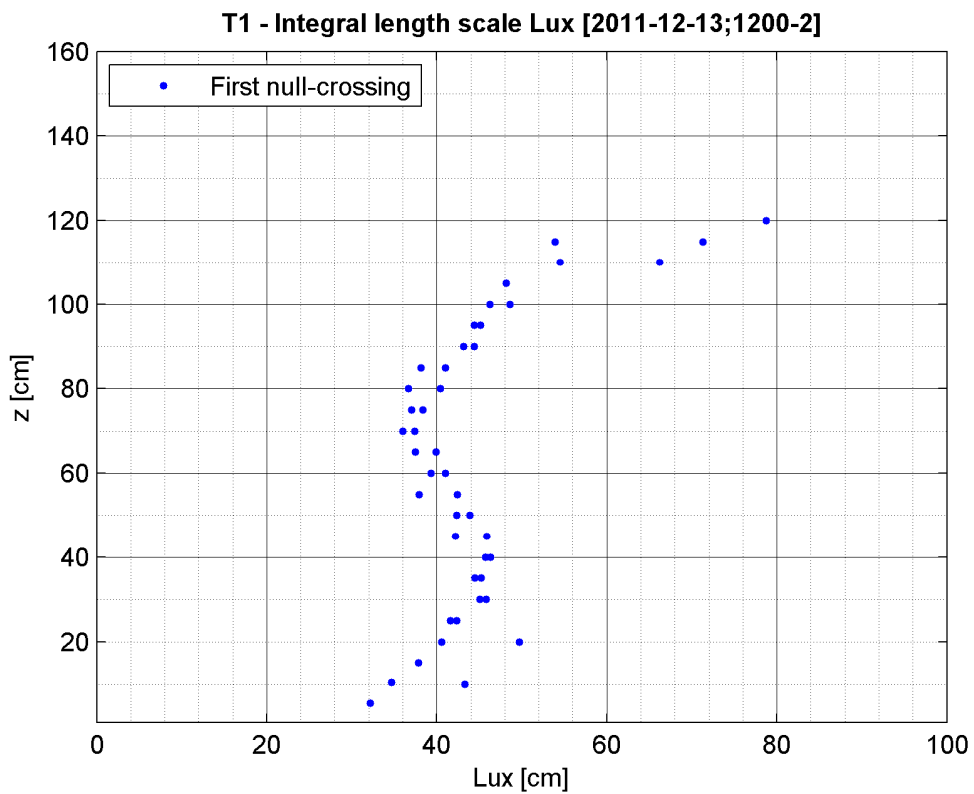


Figure 4.9 Integral length scale, L_{ux} (RAU8+collector) in the figure: first zero-crossing

Upwards

Downwards

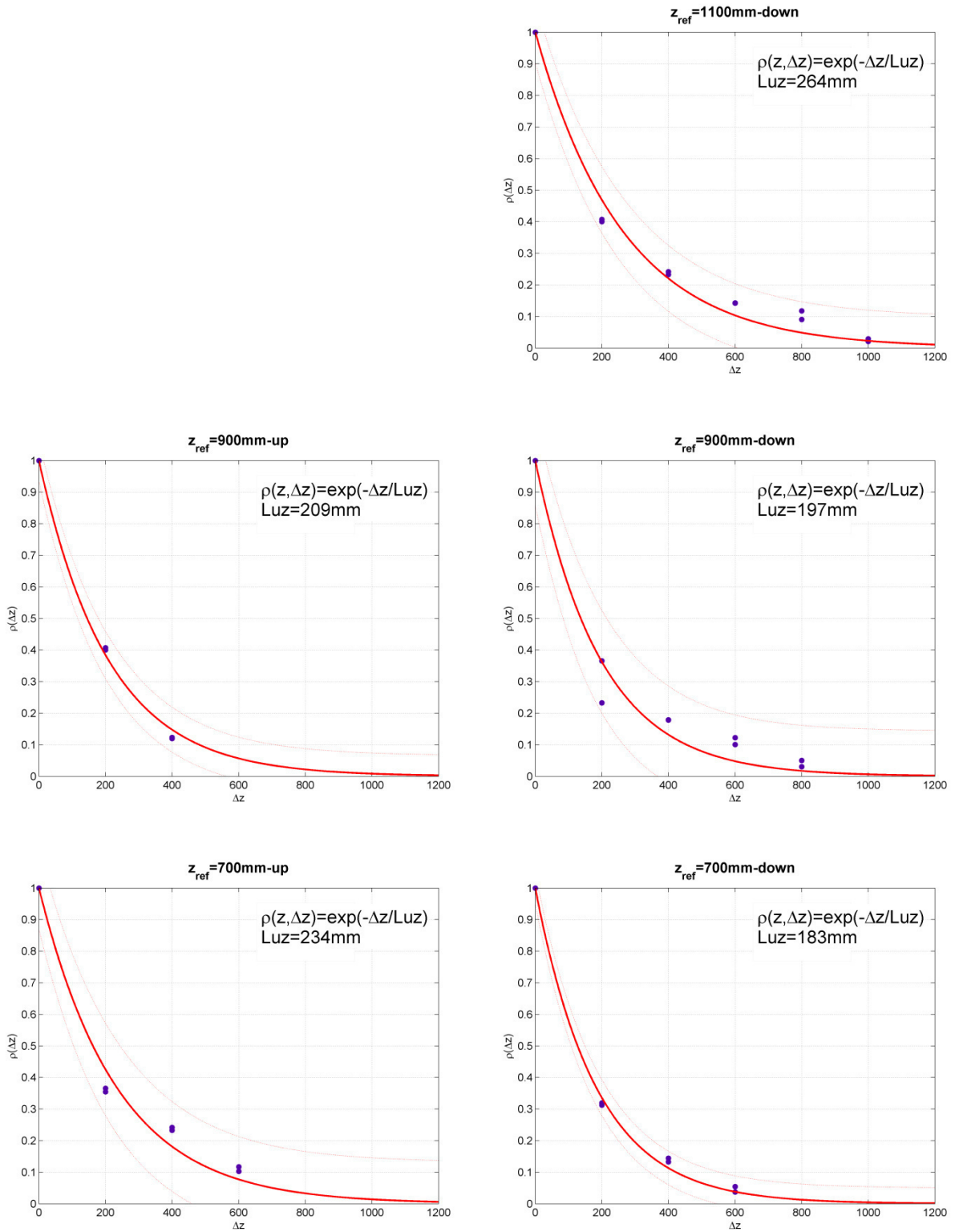


Figure 4.10 Cross-correlation coefficients $\rho_u(z, \Delta z)$ (RAU8+collector) (continued in the next page)

Upwards

Downwards

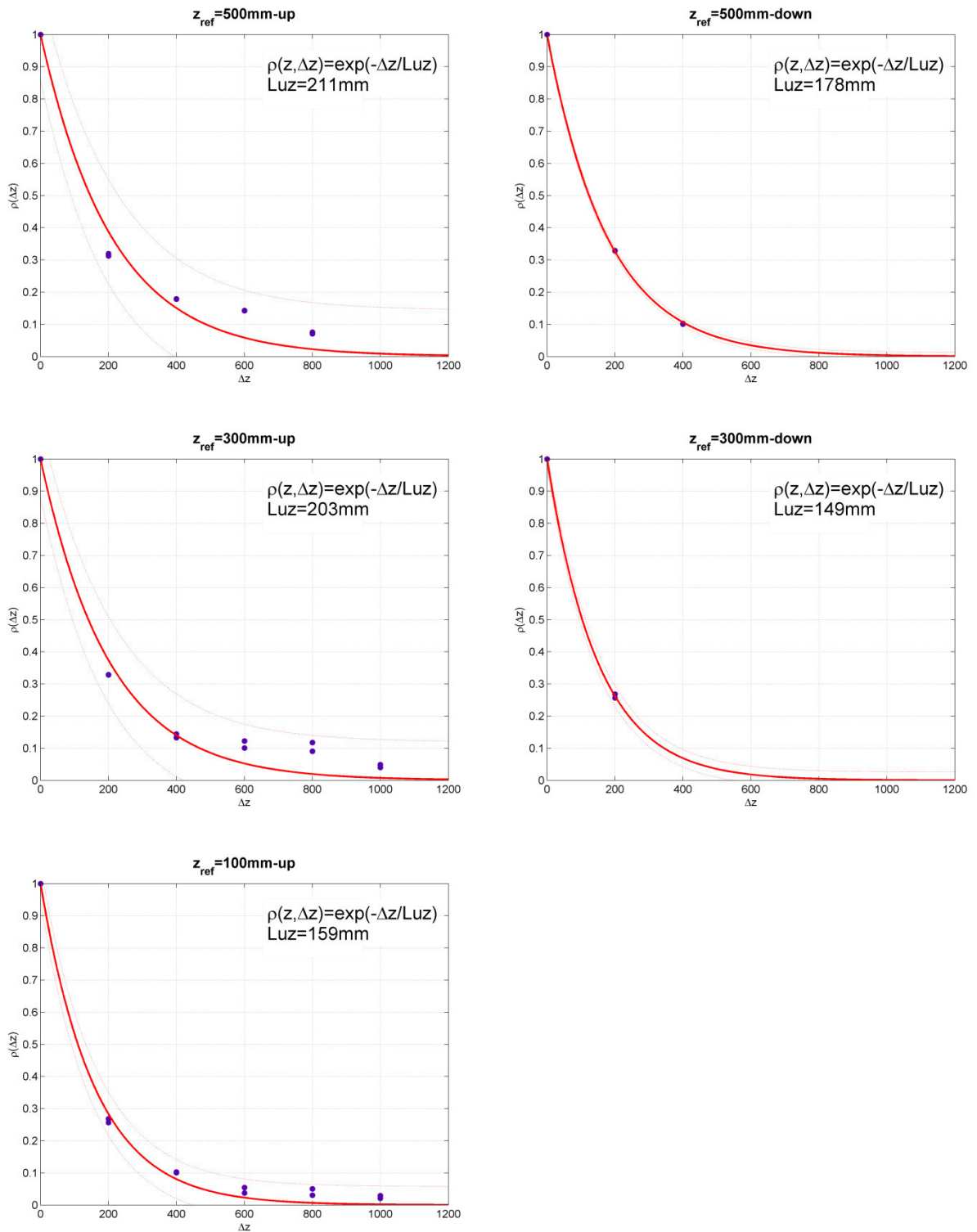


Figure 4.10 Cross-correlation coefficients $\rho_u(z, \Delta z)$ (RAU8+collector)
(continued)

The vertical scale of the u-component L_{uz} will be compared in Chapter 7 to the correlation length of pressures L_{pz} . In view of that, a representative value of L_{uz} is chosen at each level as the average of the values in the upward and downward directions. The final result is:

Table 4.2 L_{uz} (average between upward and downward directions), RAU8+collector

z [mm]	100	300	500	700	900	1100	mean
L_{uz} [mm]	159	176	194	209	203	264	200

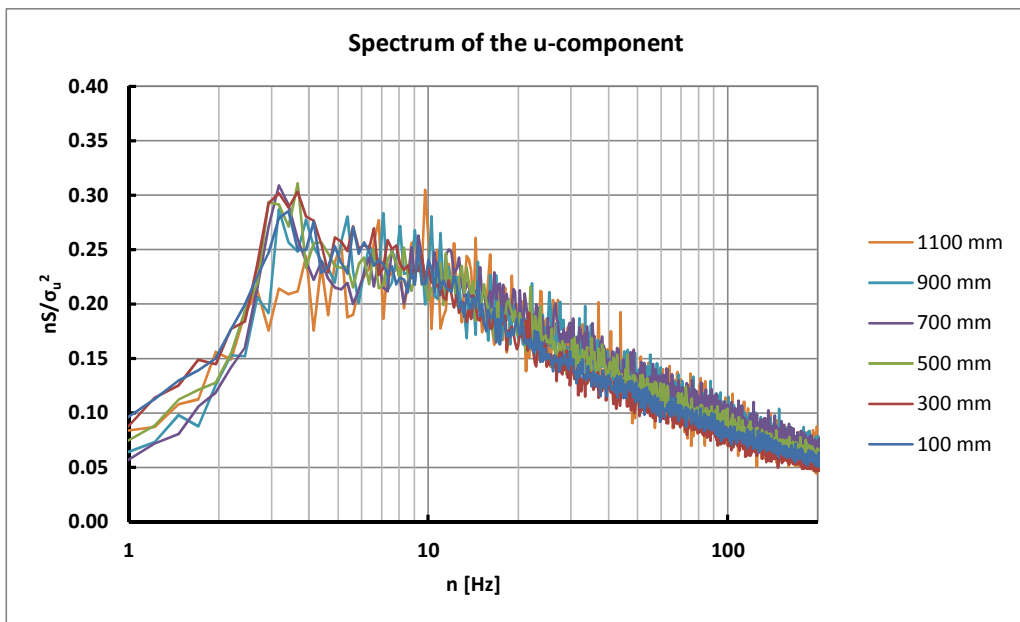


Figure 4.11 Spectra of wind fluctuations in the along-wind direction (u-component) at several levels (RAU8+collector)

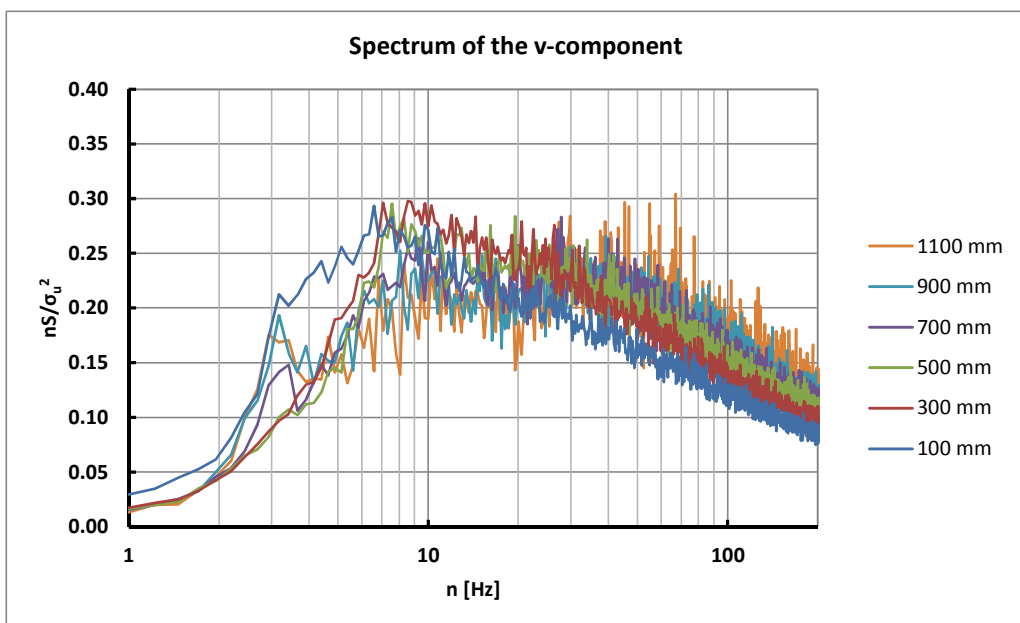


Figure 4.12 Spectra of wind fluctuations in the across-wind direction (v-component) at several levels (RAU8+collector)

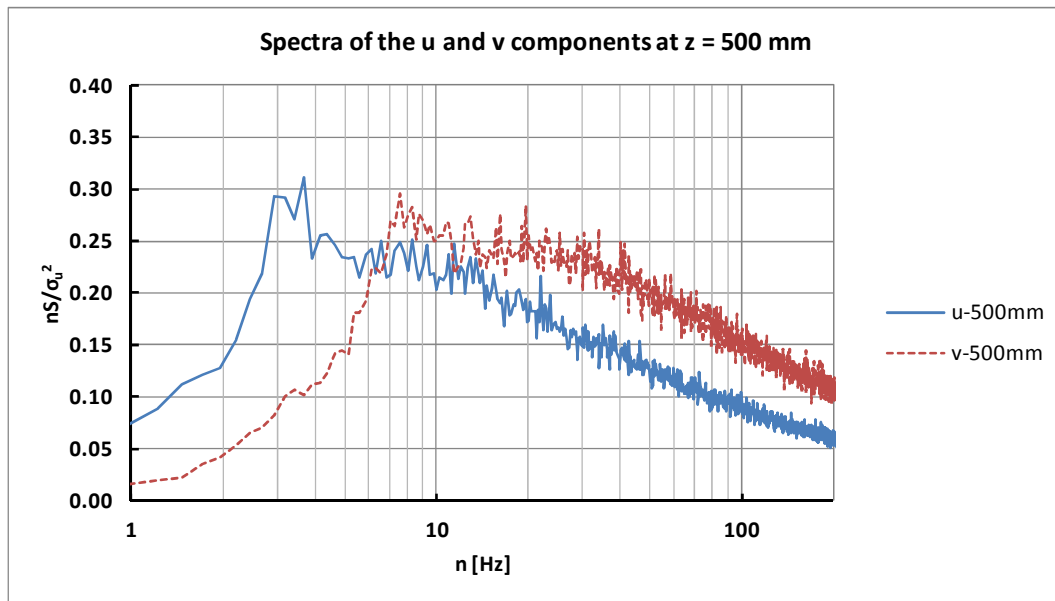


Figure 4.13 Spectra of wind fluctuations in the along-wind (*u*-component) and across-wind (*v*-component) directions at 500 mm (RAU8+collector)

The unusual peak at about 3-4 Hz in the *u*-spectrum in Figure 4.13 (detectable at higher frequencies also in the *v*-spectrum) is not produced by the slight modification of RAU8 by including the collector. It is difficult to find its precise cause. By the way, it is also recorded in pressure measurements. Once pressures are integrated along the circumference, for example to calculate the lift force, such a peak disappears in the lift spectrum because the two half lifts have negative correlation in that range of frequencies.

In any case, flow disturbances are not surprising in a wind tunnel. They can be produced by the rotor blades, the motor itself, the vibrations of the ground surface and of the wind tunnel walls or they can be electrical disturbances.

The similarity criteria between wind tunnel and full-scale require that the dimensionless parameters (e.g. S_t , Re , I_u, \dots) assume the same value in the wind tunnel and in full-scale. All the quantities which have the same dimension (for example, length, velocity or time) should be scaled according to the length scale λ_L , λ_V , λ_T , respectively. They represent the ratios between the values in the wind tunnel and the values in full-scale.

Due to the scale of the model, it is not possible in this work to reproduce in the wind tunnel the same Re as in full-scale. Its effects and the use of surface roughness in order to overcome the mismatch are discussed in section 4.4. The similarity of S_t requires that: $\lambda_L = \lambda_V * \lambda_T$.

$$S_t = \left(\frac{nD}{U} \right)_{WT} = \left(\frac{nD}{U} \right)_{FS} \rightarrow \lambda_L = \lambda_V * \lambda_T \quad (4.12)$$

If λ_L is equal to the scale of the model, i.e. 1:1000, the turbulence (in particular L_{ux}) and the boundary layer should be scaled accordingly. In fact, the full-scale value of L_{ux} is an uncertain parameter in itself. Chapter 2 proved that different codes and calculation methods provide more or less similar results in the surface layer, but very different ones in the Ekman layer. Similarly, T_{ux} can be directly calculated from wind tunnel data by equation (4.9); in full-scale it can be derived by Taylor hypothesis. The comparison between L_{ux} (T_{ux}) in the wind tunnel and in full-scale provides an estimation of the approximation, in case the data are used in a structural calculation on 1-km prototype. In any case, Figure 4.14 shows that the turbulence scale reproduced in the wind tunnel, multiplied by the scale factor 1000 ($\lambda_L = 1:1000$) is not too far from the Code predictions (even extrapolated at large heights). Instead, the H&D model would suggest much larger integral length scales, which cannot be reproduced in the wind tunnel. This partial simulation of turbulence implies, with regard to the H&D model, a smaller background response and higher dynamic amplification.

In conclusion, by assuming $\lambda_L = 1:1000$ and having $\lambda_V = 1:2.05$ ($U_{FS}(z=H) = 51.31$ m/s; $U_{WT}(z=H) = 25.07$ m/s), it results $\lambda_F = 1/488$; $\lambda_T = 488$. By looking at Figure 4.14 it can be inferred that it is not too far from the time scale that would be obtained by comparing T_{ux} in the wind tunnel and T_{ux} in full-scale.

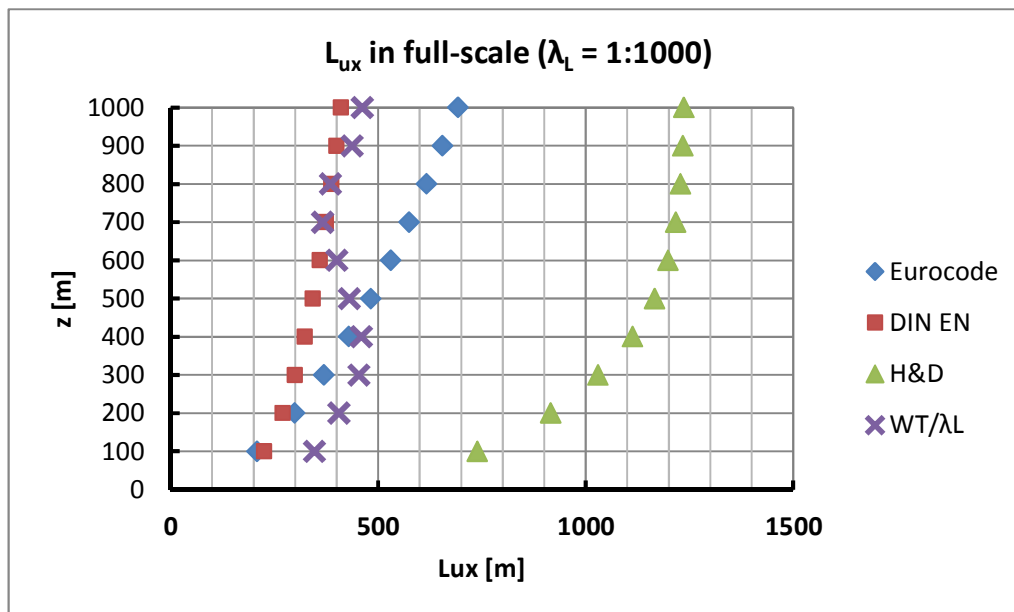


Figure 4.14 Integral length scale of turbulence L_{ux} in full-scale. The violet marks represent L_{ux} in the wind tunnel divided by the length scale factor 1:1000.

The following table summarizes the boundary layer characteristics (RAU8+collector). They are interpolated at levels of pressure measurements for further use.

z [mm]	$U_m(z)/U_{pra}$	$I_u(z)$	L_{ux} [mm]
990	0.927	0.077	459
950	0.920	0.079	448
910	0.914	0.081	440
890	0.910	0.081	429
850	0.903	0.082	396
750	0.884	0.086	377
650	0.862	0.093	387
550	0.838	0.105	402
520	0.830	0.110	425
505	0.826	0.112	429
495	0.823	0.114	432
480	0.818	0.116	437
450	0.809	0.119	440
350	0.775	0.137	448
250	0.741	0.153	419
150	0.694	0.157	379
50	0.602	0.157	322




Table 4.3 Summary: flow characteristics, RAU8+collector

Figure 4.15 RAU8+collector (WiSt wind tunnel)

Last but not least, some measurements are also done in empty tunnel. These are the characteristics of the flow:

- $U(z) \approx U_{pra}$ (uniform flow, apart from wall effects);
- $I_u \approx 5\%$
- $L_{ux} \approx 3\text{-}4$ cm (isotropic turbulence), by fitting Von Karman spectrum.

4.1.3 Pressure measurement technique

The wind tunnel facilities allow to measure 92 pressures simultaneously. The measurement chain consists of pressure sensors, amplifiers and analogic-digital (A/D) converters. The pressure sensors are four-active-element piezoresistive bridges. When a pressure is applied, a differential output voltage, proportional to that pressure, is

produced. Differential sensors provide a differential voltage proportional to the pressure differential between two ports. One port measures the wind pressure on the model, the other one is connected to the static pressure of the Prandtl tube. Two different pressure sensors are used:

- Type 1: Honeywell 170 PC
Measurement range ± 35 mbar
- Type 2: AMSYS 5812-0001-D-B
Measurement range ± 10.34 mbar

They are calibrated by using different factors, so that 5 mbar corresponds to 5 V for the type 1 (the most sensitive) and 5 mbar corresponds to 1 volt for type 2. A static calibration is performed to find pressure to voltage relations for each pressure sensor by using a Betz manometer, which allows to load the system with a known pressure.

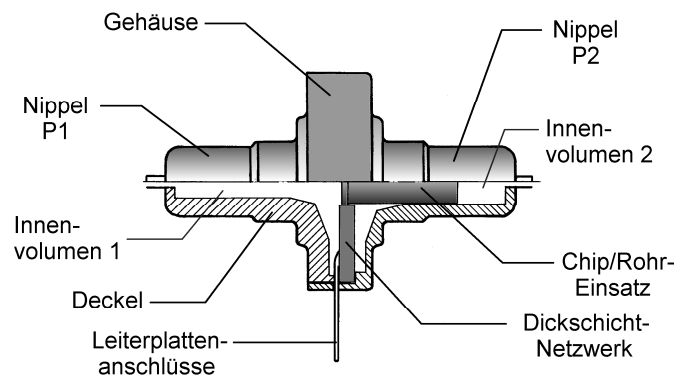


Figure 4.16 Pressure sensor Honeywell 170PC



Figure 4.17 Pressure cell AMSYS

The pressure cells AMSYS also incorporate the amplifiers. Instead, the amplifiers for the type 1 are external and independent from one another (Figure 4.18). Then, all the analogic signals are converted into a digital signal by the A/D converters. Eight cards with sixteen A/D each are available in the laboratory. The pressures are scanned in a sample-and-hold modus, which produces simultaneous sampling of the measurements. A sampling frequency of 2 kHz was selected for the measurements. The software used for recording is SBench 5.0.



Figure 4.18 External amplifiers for pressure sensors type 1

The pressure taps on the model surface are connected to the pressure sensor by a plastic tube. Special 1.5 m long tubes are used in this work, due to the dimension of the model (see section 4.2). The usual, optimized tubes of the laboratory are 60 cm in length, so they could not be used. The 1.5 m long tubes were used in previous work by Neuhaus (2009). The recorded pressures with the long tubes are corrected by a transfer function, in order to remove the dynamic effect produced by the tubes. Neuhaus (2010) explains how it is calculated. The response spectrum of the signal by using the long tube is compared to the response spectrum obtained by applying the sensor directly on the surface of a model. The latter is considered the right measurement. In fact, the transfer function is not evaluated in absolute terms, but relatively to the right measurement of the signal. The comparison shows that the tube tends to amplify the frequencies lower than 65 Hz (with maximum at about 30 Hz) and damps the frequencies higher than 65 Hz. At 200 Hz there is a damping of 50%. Therefore, the transfer function for the amplitude could be derived in the frequency domain. As regards the phase shift, it resulted to be a linear function of the frequency. Being k the slope of this linear function, the output of the pressure tubes has a constant time delay equal to $k/2\pi$. It is about 0.005 s and it is constant for each frequency, therefore no correction to the phase is applied.

The effective range in which the digital filter applied to the pressure corrects the signal is up to 200 Hz. Therefore, even if the sampling frequency is 2000 Hz, 200 Hz is the cut-off frequency. After that, the frequencies are damped. The reason for which such a high sampling frequency was chosen, despite the relatively lower cut-off frequency, is the higher accuracy in the time domain even for high-frequency (e.g. 200 Hz) fluctuations.

The time histories of pressures are acquired for a duration of $N/f_{\text{sampl}} = 2^{18}/2000 = 131.072$ s. 2^{18} is the number of time steps (N) in each recorded signal.

4.2 Model of the solar updraft tower

The model of the Solar Updraft Tower for wind tunnel tests is a circular cylinder of 1 m in height and 15 cm in diameter, made of plexiglass. The aspect ratio is about 1:7 ($H/D = 6.7$). The dimensions of the model are chosen in order not to have a too high blockage ratio. On the transversal plane the model occupies an area of $1 \times 0.15 \text{ m} = 0.15 \text{ m}^2$, while the wind tunnel cross-section is $1.8 \times 1.6 \text{ m} = 2.88 \text{ m}^2$. The ratio between the two values gives a blockage of 5%, which can be accepted without any correction of results. In scale 1:1000, the model represents a 1-km tall prototype.

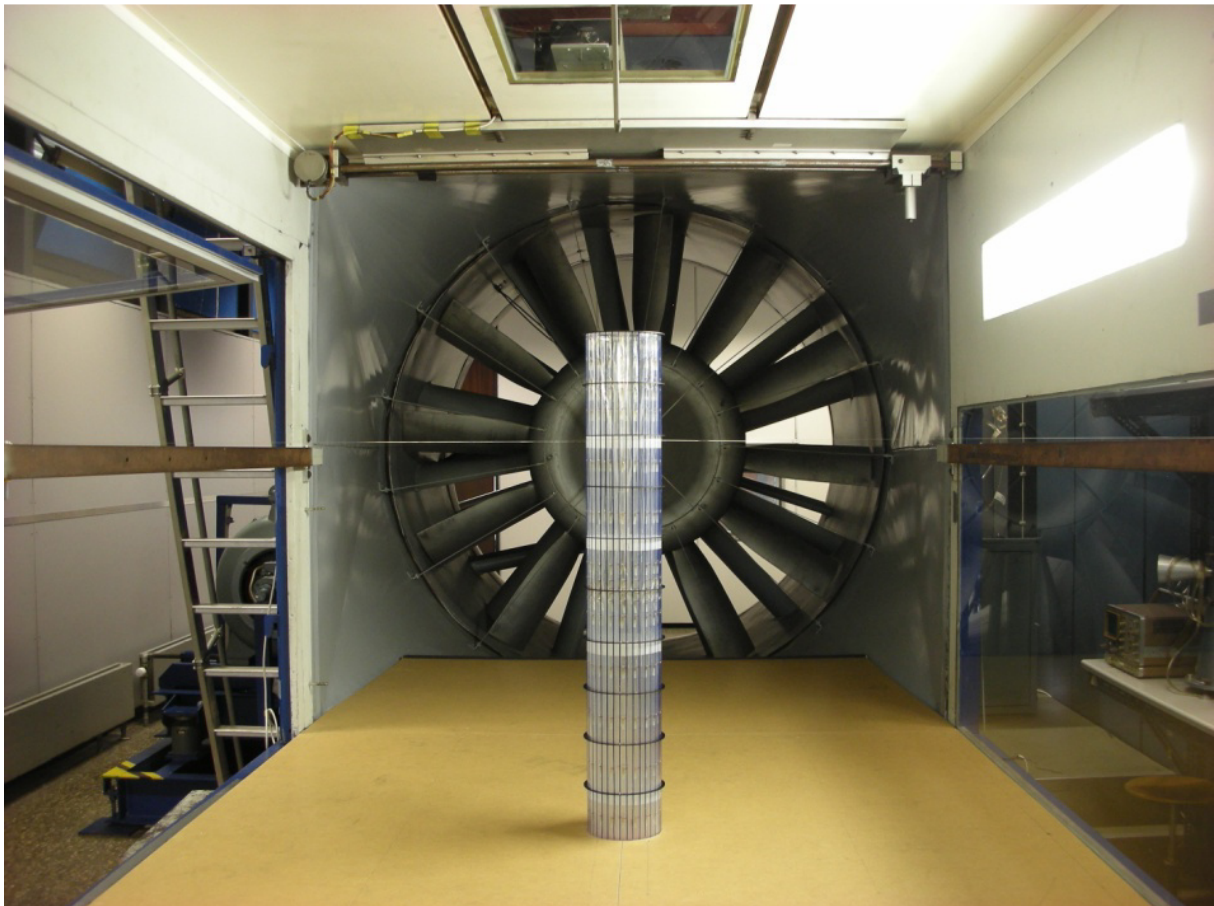


Figure 4.19 Wind tunnel model of the Solar Tower

Even though the real shape of the tower, according to the pre-designs mentioned in Chapter 1, may turn into a hyperboloid at lower levels, the wind tunnel model is a circular cylinder. This shape, which simplified the manufacturing, allows to evaluate the aerodynamic effects without any loss in generality. Moreover, the model is rigid and in order to avoid vibrations two wires³ at 800 mm fix it at the wall of the wind tunnel. The tower model is equipped with 342 pressure taps, placed at several levels along the height and in the circumferential direction, in order to investigate vertical and horizontal cross-correlations. Both external and internal pressures are measured at each level. The external pressure taps are placed at 17 levels (990-950-910-890-850-750-650-550-520-505-495-480-450-350-250-150-50 mm) at an angular distance of 20° (≈ 26 mm) at each level. The internal pressure taps in the tip region are 9 per level (angular distance = 45°) at 990 and 950 mm. Along the height (at 850-750-650-550-520-450-350-250-150-50 mm) they are 2 per level, at 0° and 180°. This is better shown in the drawing of the model (Drawing 2 on page 125).

The wind tunnel scale of the model and of the boundary layer properties reduces by around three orders of magnitude the Reynolds number from full-scale to wind tunnel conditions ($Re = UD/\nu$; $Re_{FS} \approx 50 \cdot 150 / 1.5 \cdot 10^{-5} = 5 \cdot 10^8$; $Re_{WT} \approx 30 \cdot 0.15 / 1.5 \cdot 10^{-5} = 3 \cdot 10^5$). Because of that, surface roughness (ribs) is applied along the model, in order to reproduce the same state of the flow as in full-scale. The target condition is described in the VGB guideline for cooling towers (curves K1.5-1.6). The final choice for the surface roughness – as it will be proved in section 4.4 – is $ks/D = 0.25\text{mm}/150\text{mm}$, being k the thickness of the ribs. The ribs are at an angular distance of 20°, i.e. in between two pressure taps (Figure 4.20). In any case, ribs are only applied in the scaled wind tunnel model because of Re effects, while the surface of the tower in full-scale conditions must be smooth in order to reduce the drag (Figure 3.10, Niemann, 2009).

The collector roof (4 km in diameter in full-scale) is also modeled in the wind tunnel. It is a very smooth panel in HDF, ideally representing the smooth glass surface encountered by the incoming wind (Figure 4.4). Its function in the wind tunnel is only the creation of a two-phase wind profile. The efflux inside the tower is not reproduced by means of the collector, but artificially by using the pressure difference outside-inside the wind tunnel. In fact, one of the major difficulties in the design of the model was the creation of the efflux inside the tower, due to the presence of 342 tubes inside the cylinder, which connect each measuring point on the shell to the pressure

³ The wires are too thin to modify the flow condition and disturb the measurements.

transducers. The presence of such a large number of tubes inside the tower would affect the internal flow. Moreover, the efflux had to be created somehow.

After having discussed several possibilities, it was decided to use a second circular cylinder, having a smaller diameter, to be placed inside the main cylinder representing the tower. This configuration of a pipe in a pipe allows placing all the tubes for measuring the pressures in the small cavity between the two cylinders. The two cylinders are glued together at the top through a union ring, as it can be seen in Figure 4.20.

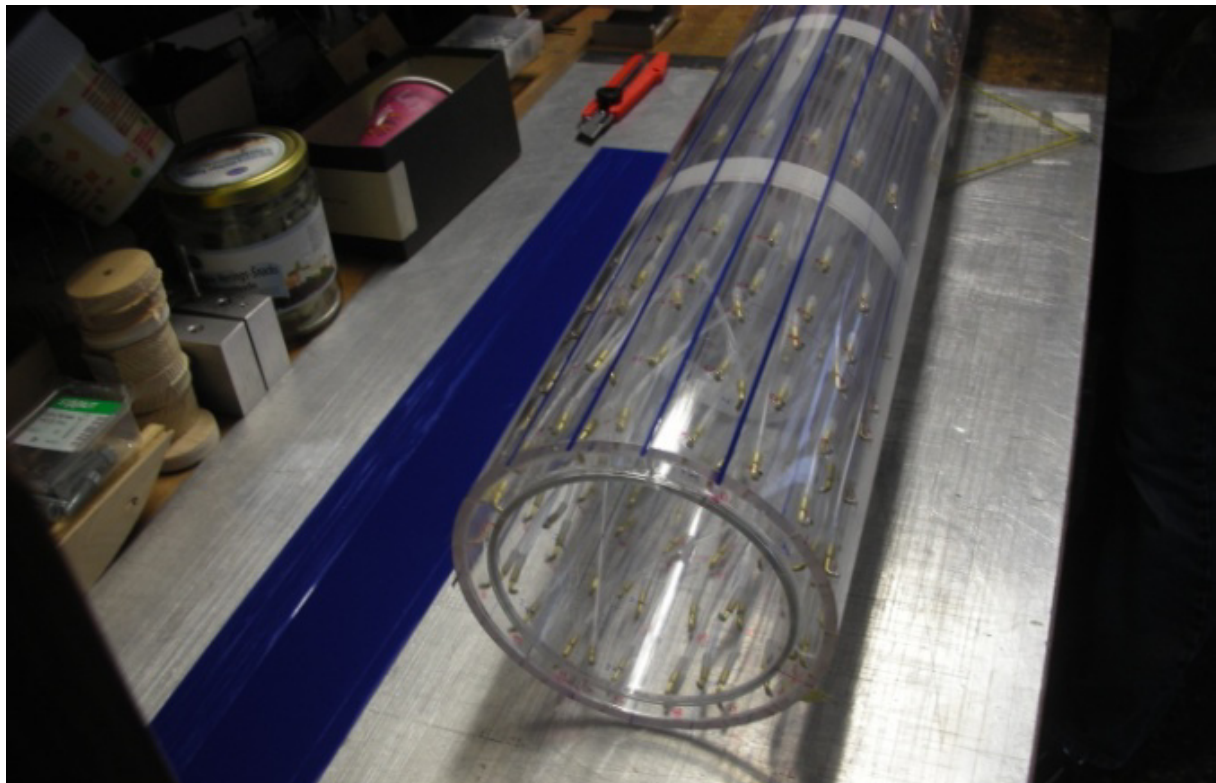


Figure 4.20 Tube-in-a-tube solution.

The outer cylinder is shorter in length than the inner one, so that the pressure tubes can come out of the model (below the wind tunnel) when the outer cylinder ends. As said, the efflux inside the tower is created by the pressure difference inside-outside the wind tunnel. In addition, a ventilator is placed below the model - at the opening of the inner cylinder - in order to achieve higher efflux velocities, if needed. Below the ventilator there is a moving plate which allows to regulate the opening, so to achieve the desired air capacity for the efflux. In addition, tests are also made in no-efflux conditions (outage condition), by closing the opening below the ventilator. Even though in reality the value of the efflux velocity during operation of the power plant depends on several conditions (e.g. the temperature rise in the collector, the pressure drop at the turbines

etc.), a quite realistic condition for the design is achieved in the wind tunnel when the velocity of the efflux inside the tower is around one half of the wind tunnel velocity. The peculiarity of the model is the presence of circular ring beams applied along the height (Figure 4.21). Tests are performed both without and with rings. The size and the number of the rings resulted to be influencing parameters of the flow around the tower. Ring beams of two sizes are tested, they are identified by the prefix SR and KR as follows:

- SR = big rings (usually called simply rings in the following): external diameter 164 mm, internal diameter 150 mm, width (w) = 7 mm $\rightarrow w/D = 7/150 = 4.67 \cdot 10^{-2}$;
- KR = small rings: external diameter 157 mm, internal diameter 150 mm, width = 3.5 mm $\rightarrow w/D = 3.5/150 = 2.33 \cdot 10^{-2}$;

They represent the highest and one of the lowest limits in the design of a solar tower. They are placed along the height at the reference distance of 10 cm in the wind tunnel scale (10 rings). Due to their strong effect on the flow, tests have also been repeated with 5 rings at a distance of 20 cm and 7 rings at a distance of about 14 cm (see section 4.3).



Figure 4.21 Ring beams along the height of the cylinder.



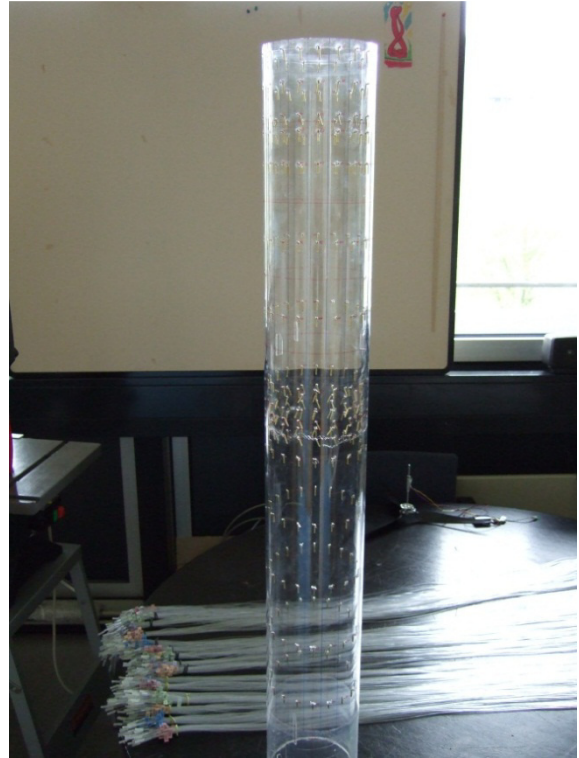
Figure 4.22 The support system for installation



Figure 4.23 Complete installation



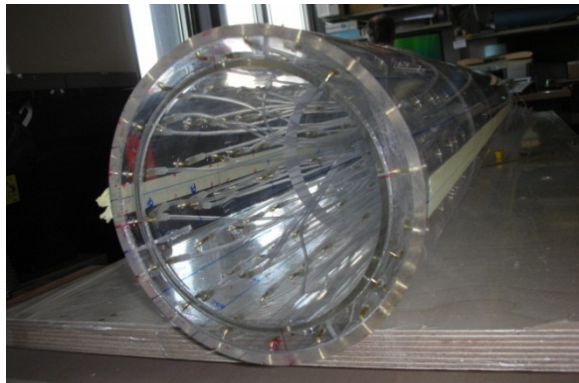
a)



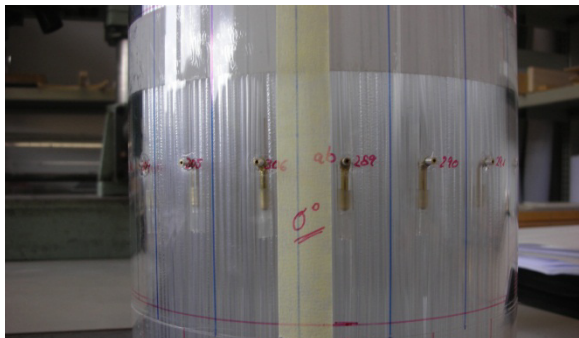
b)



c)



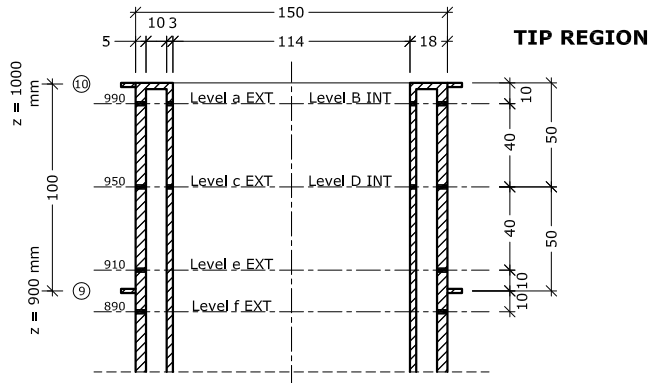
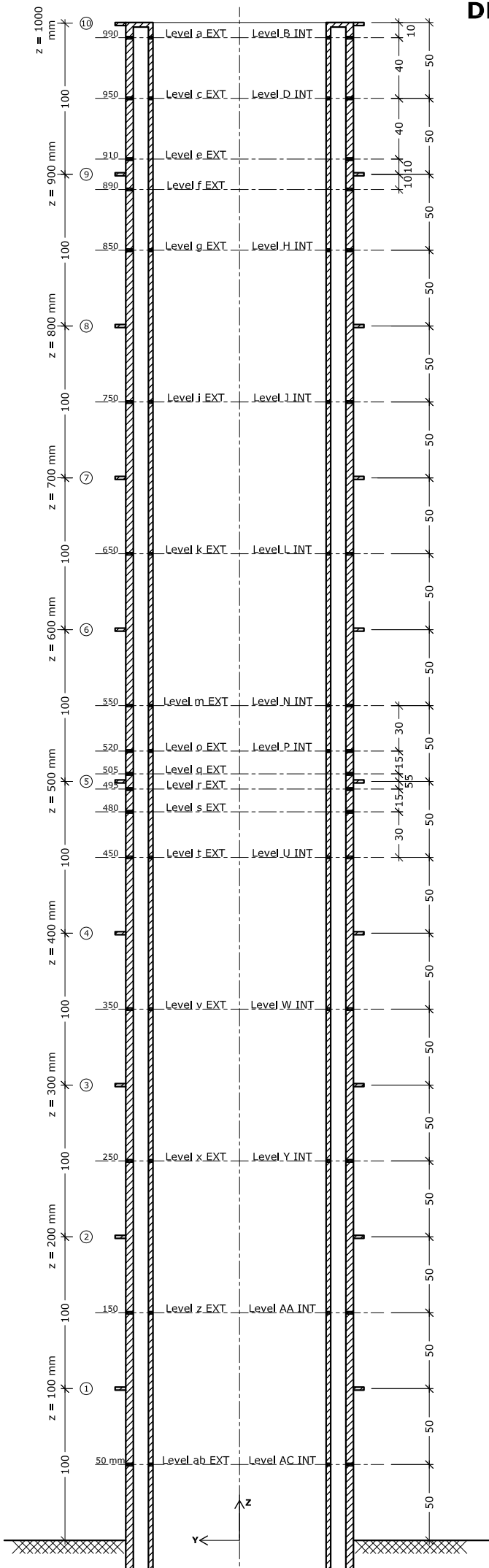
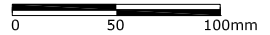
d)



e)

Figure 4.24 Model under construction: a) inner cylinder; b) outer cylinder; c) outer cylinder during application of pressure tubes; d) detail of the tip: the two cylinders are glued together; e) pressure taps and references on the outer cylinder

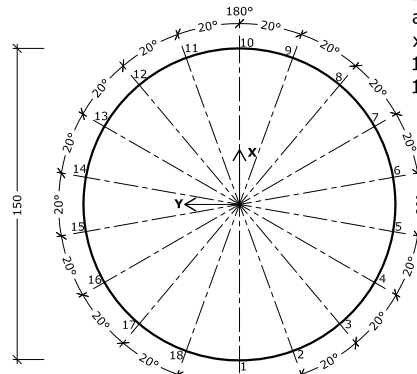
DRAWING n.2 Wind tunnel model of the solar updraft tower



HORIZONTAL DISTRIBUTION OF PRESSURE TAPS

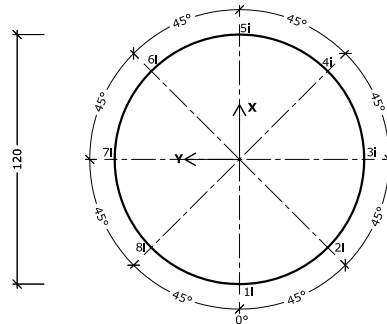
EXTERNAL PRESSURES:

Levels:
a-c-e-f-g-i-k-m-o-q-r-s-t-v
x-z-ab
18 pressure taps for each level
 $17 \times 18 = 306$



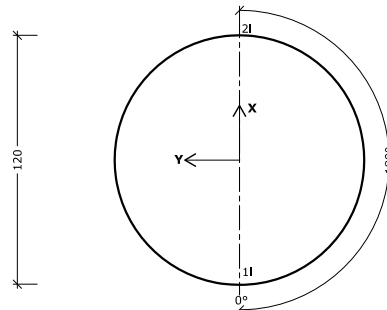
INTERNAL PRESSURES:

Levels: B-D
8 pressure taps for each level
 $2 \times 8 = 16$

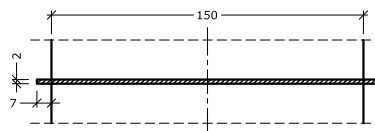


INTERNAL PRESSURES:

Levels: H-J-L-N-P-U-W-Y-AA-AC
2 pressure taps for each level
 $10 \times 2 = 20$



DETAIL OF THE STIFFENING RING



VERTICAL DISTRIBUTION OF PRESSURE TAPS

DRAWING n.3 Installation of the model and creation of efflux

Details about the model

Tower:

Height = 1 m

Outer cylinder: plexiglass, $\varnothing_{ext} = 150 \text{ mm}$, $\varnothing_{int} = 140 \text{ mm}$

Inner cylinder: plexiglass, $\varnothing_{ext} = 120 \text{ mm}$, $\varnothing_{int} = 114 \text{ mm}$

External pressure taps: 17 levels, 18 taps at each level (spacing 20°)

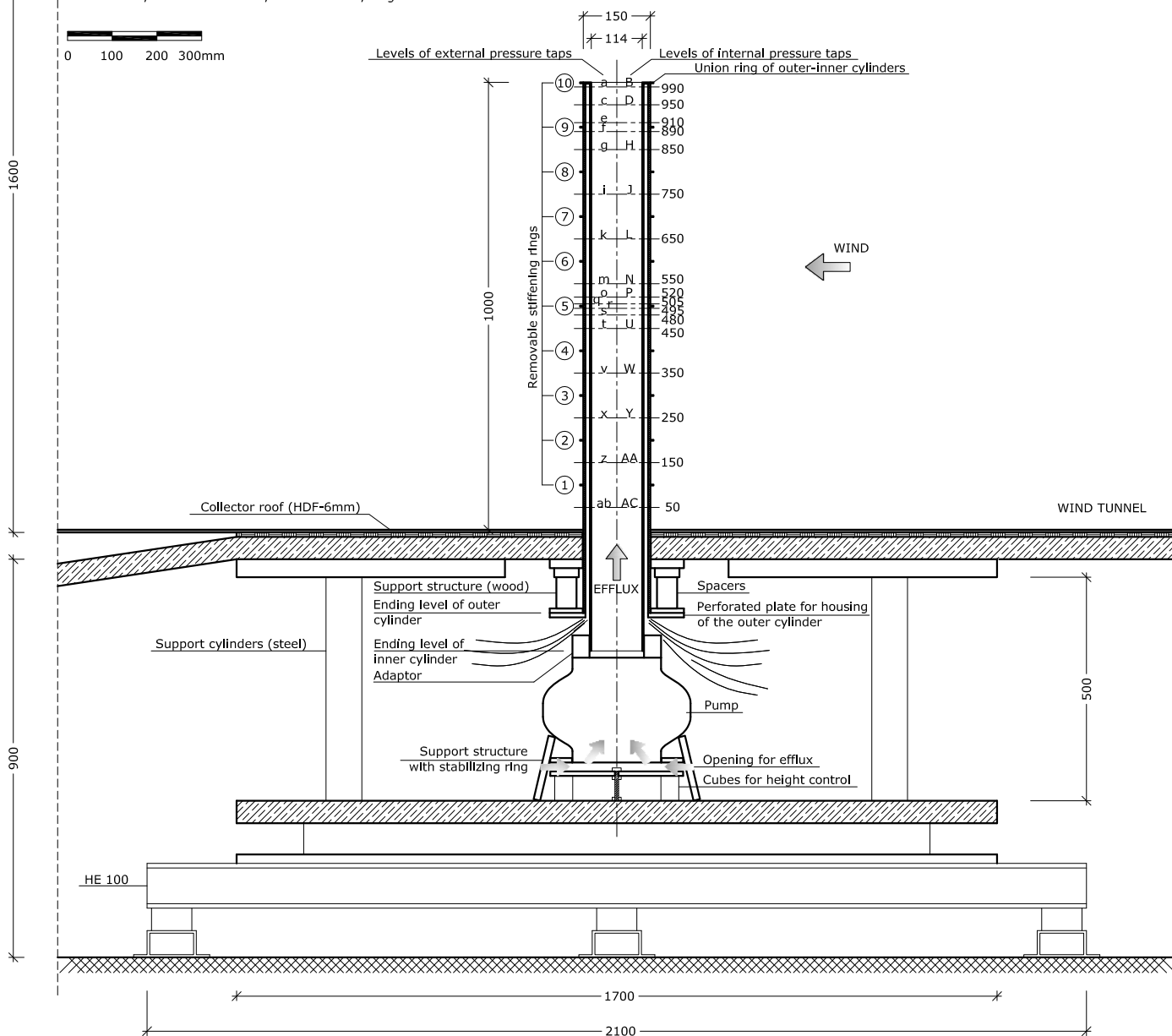
Internal pressure taps: 12 levels, 2 or 8 taps at each level

Total: 342 pressure taps

Surface roughness: ribs, spacing 20° , height = 0.25 mm

Collector:

Plate in HDF, thickness = 6 mm, width = 1.8 m, length $\approx 4 \text{ m}$



4.3 Outline of the experiments

The model of the tower without rings is the reference case to identify the flow condition and study the aerodynamic of the flow around a circular cylinder $H/D = 7$, immersed in boundary layer flow. Most of the studies in literature refer to sub-critical Re ; in addition, the aspect ratio and the characteristics of the boundary layer influence the results (Chapter 3). Therefore, before investigating the effect of the ring beams, it is necessary to have a deep knowledge of the flow around the circular cylinder without ring beams. Because of that, each test is always made twice: once with the rings, once without them. In addition, several conditions, in terms of surface roughness, flow velocity, boundary layer, efflux, number of rings, size of rings are tested. The nomenclature used in the campaign is described in the following:

1. Boundary layer:

- T1 = boundary layer flow RAU8 + collector;
- T3 = uniform flow (empty tunnel);

2. Surface roughness conditions on the outer surface of the model:

- R0 = smooth cylinder;
- R1 = ribs at a spacing of 20° , $k_s = 0.250$ mm ($k_s/D = 1.67 \cdot 10^{-3}$);
- R2 = ribs at a spacing of 10° , $k_s = 0.250$ mm ($k_s/D = 1.67 \cdot 10^{-3}$);
- R3 = ribs at a spacing of 20° , $k_s = 0.375$ mm ($k_s/D = 2.50 \cdot 10^{-3}$);
- R4 = ribs at a spacing of 10° , $k_s = 0.375$ mm ($k_s/D = 2.50 \cdot 10^{-3}$);
- R5 = ribs at a spacing of 20° , $k_s = 0.500$ mm ($k_s/D = 3.33 \cdot 10^{-3}$);

The surface roughness is always made of ribs. This choice is motivated by simplicity of manufacturing and consolidated experience on cooling towers (VGB, 2010).

3. Wind tunnel velocity: for practical reasons, the wind tunnel velocity to be used in each test is identified by the number of rounds per minute (rpm) of the fan. Depending on the static pressure and on the temperature during measurements, the density of air and consequently the velocity may change. A small difference in the measured velocity corresponding to the same rpm is also noted in presence or absence of boundary layer (RAU8 or empty tunnel) and in presence or absence of efflux in the chimney. Approximately, it results:

- 100 rpm; $U_{\text{pra}} \approx 3$ m/s
- 200 rpm; $U_{\text{pra}} \approx 5$ m/s

- 400 rpm; $U_{\text{pra}} \approx 8 \text{ m/s}$
- 600 rpm; $U_{\text{pra}} \approx 12 \text{ m/s}$
- 800 rpm; $U_{\text{pra}} \approx 16 \text{ m/s}$
- 1000 rpm; $U_{\text{pra}} \approx 20 \text{ m/s}$
- 1250 rpm; $U_{\text{pra}} \approx 25 \text{ m/s}$
- 1400 rpm; $U_{\text{pra}} \approx 27 \text{ m/s}$

1400 rpm is the highest velocity which was used, although the capacity of the wind tunnel was even higher, up to 1500 rpm. However, the resulting pressure at higher wind speed would have exceeded the sensitivity range of the pressure transducers type 2, which could not be regulated.

The low velocity range 100-200-400 rpm is tested only on the smooth cylinder, in the hope to reach subcritical conditions (laminar separation). However, at very low speed the wind tunnel velocity was not always stable.

4. Efflux condition:

- EF0 = no efflux;
- EF1 = efflux;

The velocity of the efflux is regulated at about one half of the wind tunnel velocity (section 4.4.1).

5. Effect of ring beams:

- SR0 = no rings;
- SR1 = ten big rings along the height, equally spaced at a distance of 10 cm;
- SR7 = seven big rings along the height, equally spaced at a distance of 14 cm (15 cm in the two lowest compartment);
- SR5 = five big rings along the height, equally spaced at a distance of 20 cm;
- KR1 = ten small rings along the height, equally spaced at a distance of 10 cm;
- KR7 = seven small rings along the height, equally spaced at a distance of 14 cm (15 cm in the two lowest compartment);
- KR5 = five small rings along the height, equally spaced at a distance of 20 cm;

The wind tunnel equipment allows to measure maximum 92 pressures simultaneously. However, some sensors were out of use at the time of the tests, therefore no more than four levels (with 18 pressure taps each, on the external surface) could be measured at the same time, plus other positions at proper convenience. In the first plan of the experiments, it was decided to measure all the correlations of the 342 pressure taps in the basic conditions: T1(&T3)-SR0&SR1-EF0(&EF1)-R1, where the nomenclature out of brackets had the priority. In order to measure all the cross-correlation, the pressures had to be divided into groups and each group had to be measured with all the other ones. However, due to the appearance of the new phenomenon described in Chapter 5 – during the second set of measurements (May 2011) – the original plan of experiments was revised. Different experimental conditions had to be tested for a deeper understanding of the phenomenon: not only SR0 and SR1, but also SR5, SR7, KR1, KR5, KR7; not only R1, but also R0-R2-R3-R4-R5. Consequently, the complete correlation field could not be measured, but only the most important pressures were measured simultaneously.

In summary, the following series of measurements were defined (only pressures on external surface and complete circumference are mentioned):

- MS01: levels $z = 990-950-910-890$ mm;
- MS02: levels $z = 910-890-850-750$ mm;
- MS03: levels $z = 750-650-550$ mm;
- MS04: levels $z = 550-520-505-495$ mm;
- MS05: levels $z = 505-495-480-450$ mm;
- MS06: levels $z = 450-350-250-150$ mm;
- MS07: levels $z = 250-150-50$ mm + vertical at 0° ;
- MS08: levels $z = 990-950-750$ mm;
- MS09: levels $z = 550-450$ mm;
- MS10: levels $z = 450-50$ mm + vertical at 80° ;
- MS28: verticals at $20^\circ, 120^\circ, 180^\circ, 300^\circ$;
- MS30/MS32: levels $z = 950-850-750-650$ mm;
- MS31: levels $z = 950, 890, 750, 650$ mm;
- MS33: levels $z = 950-910-890-850$ mm;
- MS34: levels $z = 650-550-520-480$ mm;

The experimental campaign was articulated in the following four sets, which became necessary as the investigation was proceeding:

Set n.1 (April 2011):

Turbulence setting: T1
Rings: SR0
Efflux: EF0/EF1
Surface roughness: R1
Wind tunnel velocity (rpm): 600/800/1000/1250/1400
Measurement series: MS01/02/03/04/05/06/07/08/09/10/28;

Set n.2 (May 2011):

Turbulence setting: T3
Rings: SR0/SR1
Efflux: EF0/EF1
Surface roughness: R1
Wind tunnel velocity (rpm): 0600/0800/1000/1100/1250/1400
Measurement series: MS01/02/04/05/08/09;

Set n.3 (October 2011):

Turbulence setting: T1
Rings: SR0/SR1/SR7/SR5/KR1/KR7/KR5
Efflux: EF0/EF1
Surface roughness: R0/R1/R2/R3/R4/R5
Wind tunnel velocity (rpm): 0600/0800/1000/1250/1400
Measurement series: MS30/31;

Set n.4 (December 2011):

Turbulence setting: T1
Rings: SR0/SR1
Efflux: EF0/EF1
Surface roughness: R1/R3
Wind tunnel velocity (rpm): 0600/0800/1000/1250/1400
Measurement series: MS32/33/34;

4.4 Preliminary results on the circular cylinder

In this section, preliminary results on the cylinder without rings are presented.

4.4.1 Velocity of efflux

The tests are performed in two conditions: open efflux (EF1) and closed efflux (EF0). The latter represents the condition of out of use of the power plant. For many aspects, EF0 is more dangerous than EF1. In particular, the tip effect in EF0 is stronger. In the condition of open efflux, the tests are performed with only one efflux velocity. The influence of different efflux velocities on the pressures is not investigated. The efflux velocity which acts in EF1 is around one half of the undisturbed flow velocity (U_{pra}). This is achieved in the experiments by defining a proper opening below the model, through the position of the wooden plate under the ventilator (Figure 4.23).

The efflux velocity was measured during a preliminary test by a second Prandtl tube placed inside the chimney close to the tip. Figure 4.25 shows the ratio between the Prandtl velocity U_{pra} and the efflux velocity at different U_{pra} , corresponding to a certain position of the wooden plate used in all the experiments.

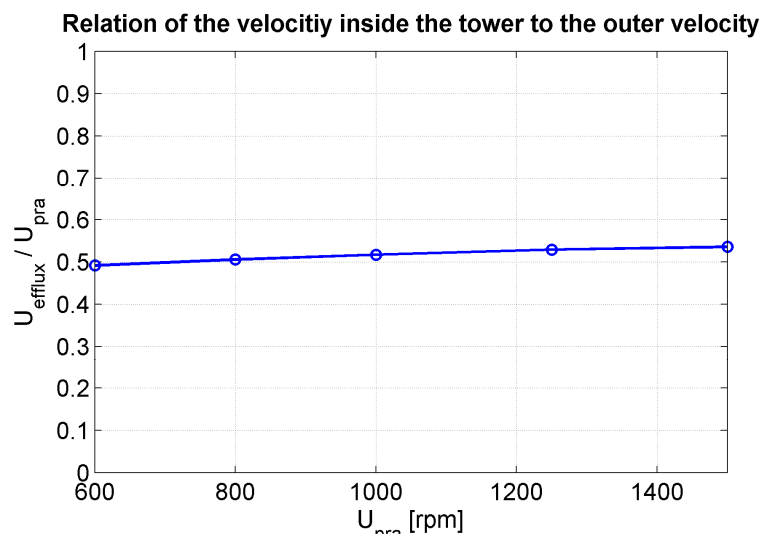


Figure 4.25 Efflux velocity

The effect of the efflux on the pressures is evident in the tip region, while it is not influent at lower levels. Figure 4.26 shows the modification of the external pressures at $z/H = 0.95$ due to the efflux. In EF1 the lateral suction is reduced and the separation point is shifted downstream. Moreover, the increase in suction in the wake of the cylinder, around $\varphi = 150^\circ$ in EF0, due to tip vortices as explained in Chapter 3, is missing in EF1. It is then confirmed (Gould et al., 1968) that the efflux displaces the tip vortices. The peak of pressure in the wake due to the entrainment of the flow is also leveled out in EF1, as expected.

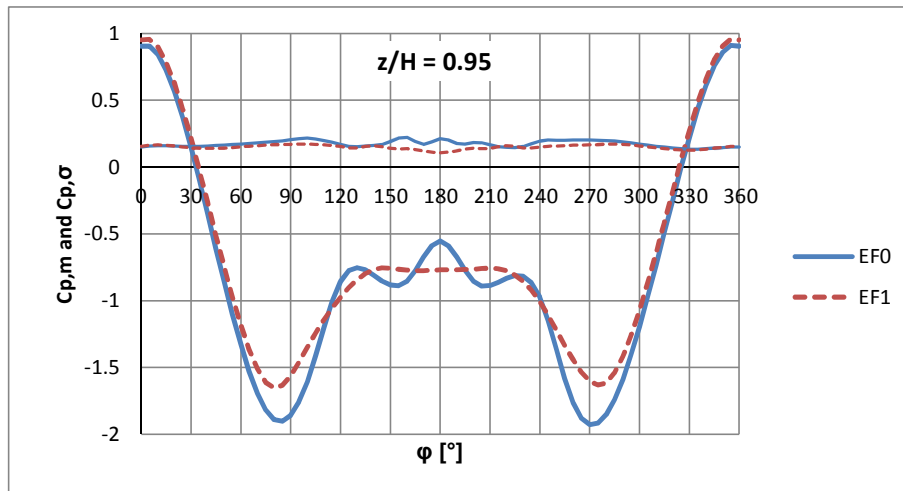


Figure 4.26 $C_{p,m}$ and $C_{p,\sigma}$ in the tip region ($z/H = 0.95$): influence of efflux.

4.4.2 Internal pressure

The internal pressure coefficient C_{pi} is calculated with reference to the velocity pressure at $z = H$. The pressure coefficient is higher in case of efflux, both in the mean as well as in the rms. Its value is approximately constant along the height and along the circumference. Only close to the tip it exhibits some variation. In any case, the value of C_{pi} is lower than the typical value for cooling towers ($C_{pi} = -0.5$ in VGB, 2010).

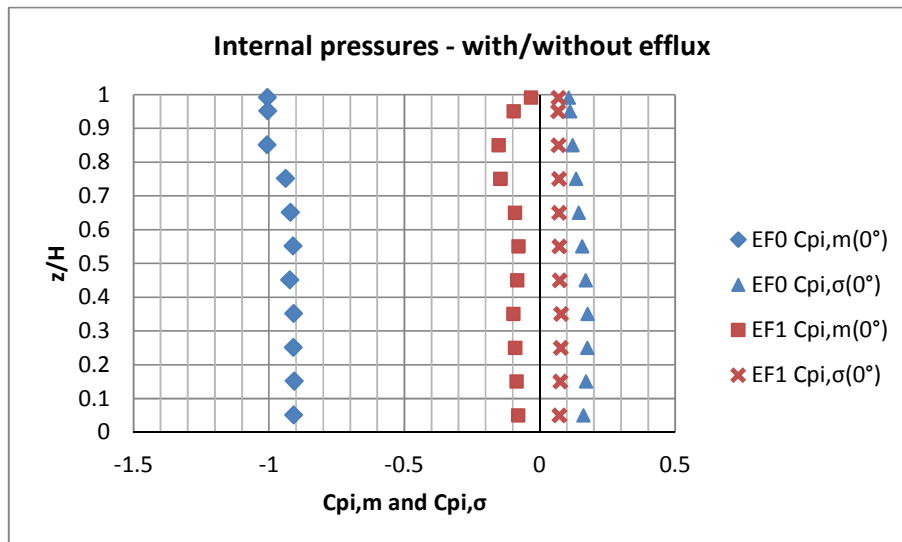


Figure 4.27 Internal pressures – spanwise variation

In absence of efflux, the internal pressure is somewhat higher at $z/H = 0.99$, $\phi = 180^\circ$, probably due to an entrainment of fluid inside the cylinder (Figure 4.28). However, the level $z/H = 0.95$ is already unaffected and the internal pressure does not show any circumferential variation.

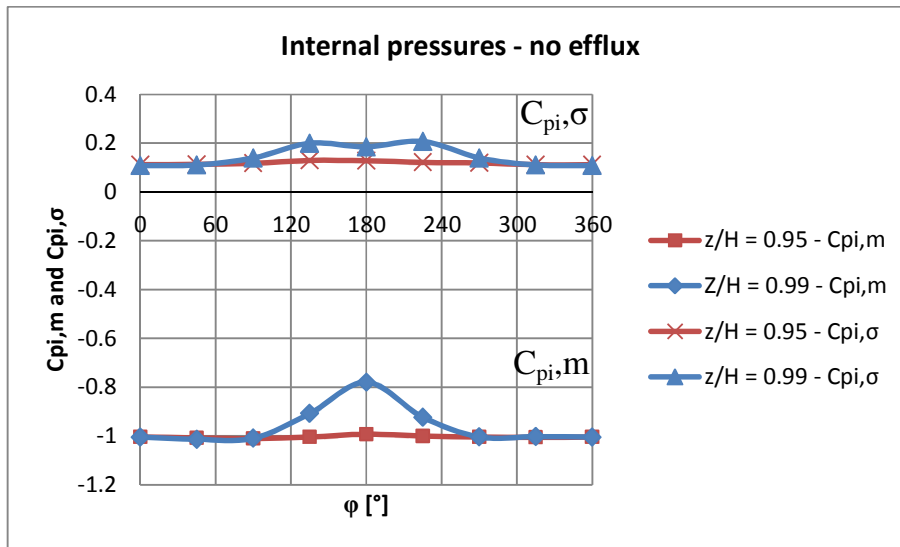


Figure 4.28 Internal pressures – circumferential variation

4.4.3 Reynolds effects on the smooth and rough cylinder

As mentioned before, due to the reduced scale of the model in the wind tunnel, the Reynolds number is around three orders of magnitude lower than in full-scale ($Re = UD/v$; $Re_{FS} \approx 50 \cdot 150 / 1.5 \cdot 10^{-5} = 5 \cdot 10^8$; $Re_{WT} \approx 30 \cdot 0.15 / 1.5 \cdot 10^{-5} = 3 \cdot 10^5$). Because of that, surface roughness (consisting of ribs) is applied to the model. The effect of surface roughness on the circular cylinder in the wind tunnel is studied with regard to the following key parameters:

- $C_{D,m}$ = mean value of the drag coefficient;
- $C_{D,\sigma}$ and $C_{L,\sigma}$ = rms values of the drag and lift coefficients;
- $C_{p,min}$ = minimum pressure (lateral suction);
- $C_{p,b}$ = base pressure;
- $C_{p,b} - C_{p,min}$ = pressure rise to separation or pressure recovery;

Further comments concern the Strouhal number (S_t) and the angle of separation.

At first, the results are presented for the level $z/H = 0.65$, which is out of the tip region, approximately in the two-dimensional normal range and available in most of the tests. Then, the spanwise variation is considered. The tests are in turbulent boundary layer (T1), unless differently specified, and only results in EF0 are reported. The Reynolds number is uniquely defined with respect to the local velocity at the tower top (at $z = H$). The dependency of air viscosity on the temperature is neglected; the value $\nu = 1.5 \cdot 10^{-5}$ at 20°C is used.

Figure 4.29 plots the drag coefficient distribution at $z/H = 0.65$ for different Reynolds numbers (i.e. different wind tunnel velocities) and for different surface roughness conditions. The blue curve (R0) refers to the smooth cylinder (according to the nomenclature in section 4.3). It can be seen that the flow around the smooth cylinder is at first in the critical state, characterized by the fall of C_D until the minimum at $Re_{cr} \approx 1.9 \cdot 10^5$. After that, the horizontal plateau is typical of the supercritical range for smooth cylinders, according to Roshko's classification (Chapter 3). On the rough cylinder in turbulent boundary layer flow (T1), for any type of surface roughness (R1-R5) the state of the flow is already beyond the critical Re . This is not only due to the surface roughness, but it is also enhanced by the turbulence of the flow. In fact, it is interesting to compare these results to the black dashed line in the figure, which is the only one referring to uniform flow and lower I_u (empty tunnel). However, due to lack of data, it is at $z/H = 0.55$. In any case, it can be seen that at high (effective) Re the effect of turbulence on the drag coefficient is limited, while it is stronger at low Re : in empty tunnel the flow around the rough cylinder R1 undergoes the critical state at $Re \approx 1.5 \cdot 10^5$. Moreover, the figure shows a certain similarity between the curves R2-R3 and R4-R5 for the whole range of Reynolds numbers. R2 and R4 have, with respect to R3 and R5, a double number of ribs with smaller height. Therefore, within a certain limit, the height of the rib and their distance act in the same manner.

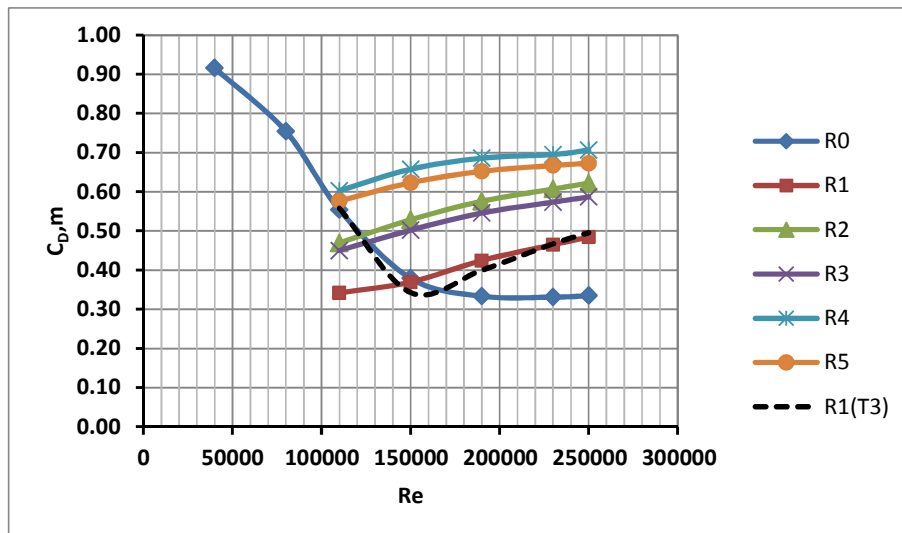


Figure 4.29 Drag coefficient vs Re ($z/H = 0.65$, R0-R5, T1 unless differently specified)

The rms values of both drag and lift coefficients on the rough cylinder do not show a large variability with Re (Figure 4.30 and Figure 4.31). The along wind fluctuations tend to increase with higher roughness. It is not surprising that in empty tunnel (black dashed line) the force fluctuations, especially in the along wind direction ($C_{D,\sigma}$), are lower, because turbulence is lower.

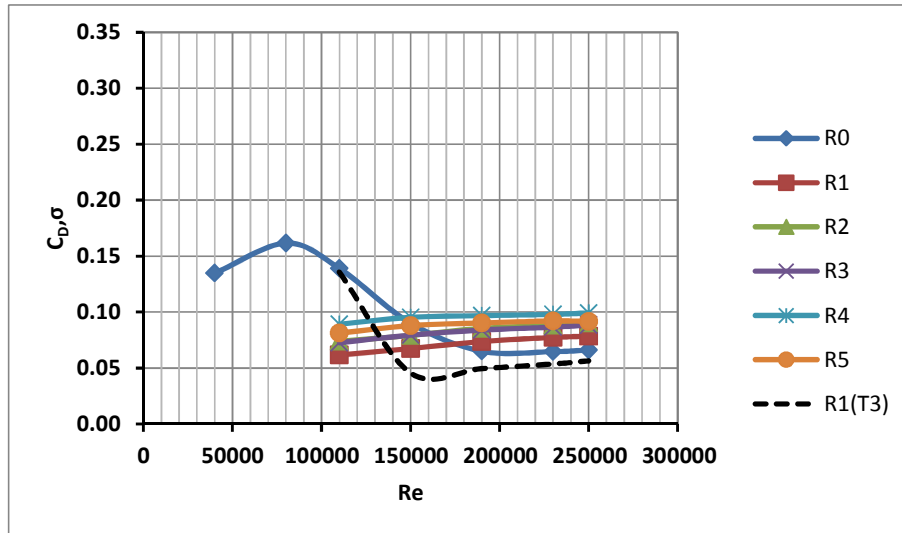


Figure 4.30 Rms drag coefficient vs Re ($z/H = 0.65$, R0-R5, T1 unless differently specified)

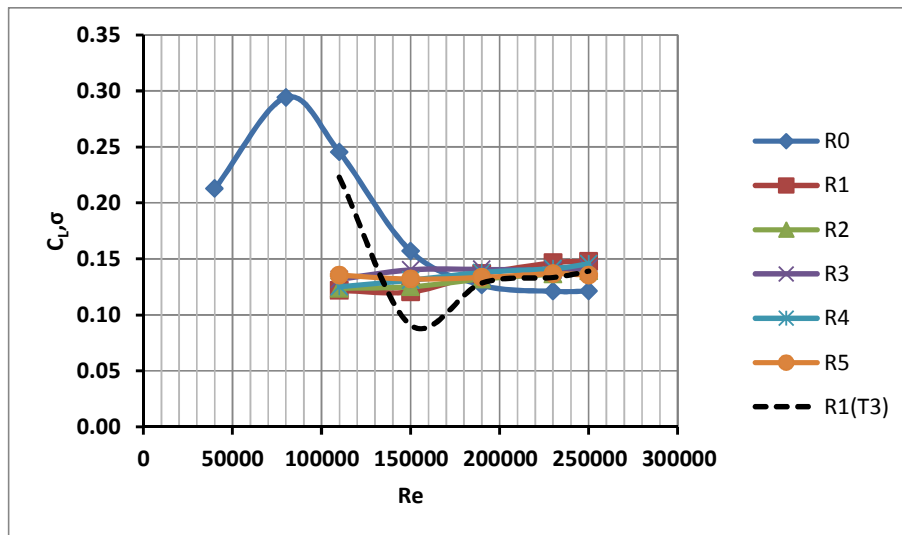


Figure 4.31 Rms lift coefficient vs Re ($z/H = 0.65$, R0-R5, T1 unless differently specified)

Figure 4.32, Figure 4.33 and Figure 4.34 complete the set of information by plotting the pressure recovery, the wake pressure and the minimum pressure, respectively.

On the smooth cylinder (R0) at $Re_{cr} \approx 1.9 \cdot 10^5$, the blue curve reaches the maximum base pressure (the lowest wake suction) and the minimum pressure at the flanges. This corresponds to the largest value of pressure recovery, which is associated to the minimum drag. After that, the horizontal plateau in the supercritical range is confirmed. All of that is in accordance to literature (Chapter 3).

On the rough cylinder, the positive rise in terms of $C_{D,m}$ (Figure 4.29) corresponds to a decrease in the pressure recovery. It is due to the progressive increase in wake suction (which rises the drag) and decrease in lateral suction. In fact, according to Güven et al. (1980), the overall effect of surface roughness on the pressure distribution is best seen in the behaviour of the pressure rise to separation or pressure recovery $C_{p,b} - C_{p,min}$. Such a parameter, which includes both variations of the base and minimum pressures

and shows opposite trend with respect to the drag, is especially important because it is almost insensitive to the effects of influencing parameters such as tunnel blockage, aspect ratio and even free-end effects. Furthermore, as explained by Güven et al. (1980), in the supercritical Reynolds number range, $C_{p,b}-C_{p,min}$ decreases with increasing Re for a given relative roughness and decreases with increasing relative roughness for a given Re number. The incremental changes in $C_{p,b}-C_{p,min}$ decrease with increasing roughness. Such a pressure difference is closely related to the characteristic of the boundary layer prior to separation and it is the reason for its strong dependence on surface roughness. All of that is confirmed by Figure 4.32.

The black curves of the rough cylinder in empty tunnel (R1-T3) confirm the critical Re at $\approx 1.5 \cdot 10^5$. This represents a point of maximum of the pressure recovery. In fact, in the critical range before Re_{cr} the pressure recovery is a small value due to the early laminar separation. At high Re , the turbulence intensity has a negligible effect on the state of the flow, as it was shown by C_D .

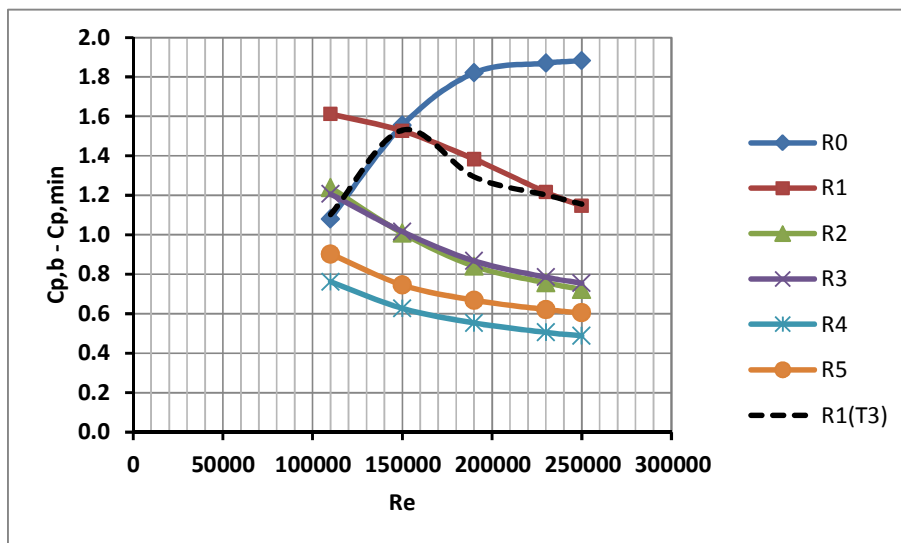


Figure 4.32
Pressure recovery
($z/H = 0.65$, R0-R5,
T1 unless differently
specified)

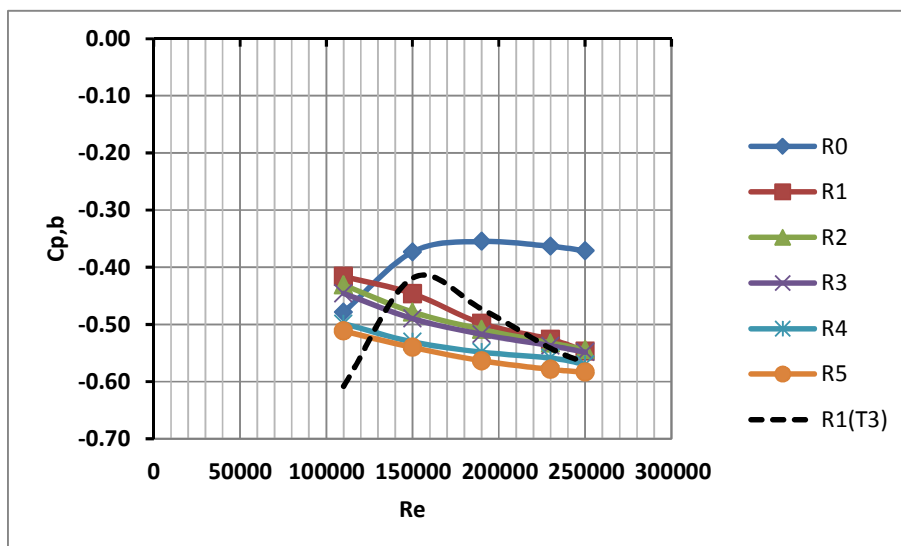


Figure 4.33 Base
pressure ($z/H =$
0.65, R0-R5, T1
unless differently
specified)

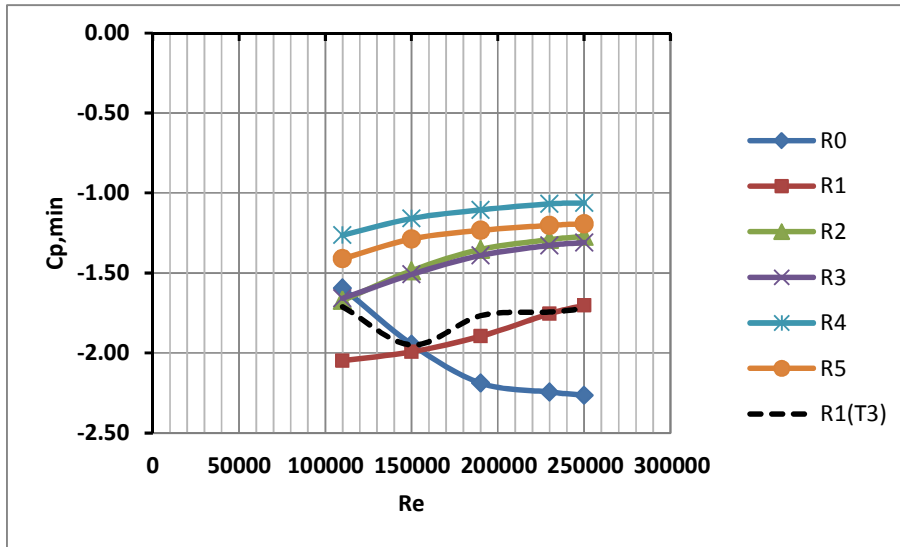


Figure 4.34 Minimum pressure at the flanges ($z/H = 0.65$, R0-R5, T1 unless differently specified)

The following figures show an overview of the variation of the mean pressure distribution with Re and surface roughness. On the smooth cylinder (R0) in Figure 4.35, it is clear that the increase in wind tunnel velocity progressively increases lateral suction and decreases wake suction. The blue and the red curves in the figure lie in the critical range (which is characterized by the fall in the drag). The critical condition is reached at first by the green curve ($Re = 1.9 \cdot 10^5$) and all the other curves collapse on that one, due to the horizontal plateau in the supercritical range. On the rough cylinder R1 (Figure 4.36), instead, the progressive increase in the Re is marked by decrease in lateral suction, accompanied by upstream movement of the separation point and increase in wake suction.

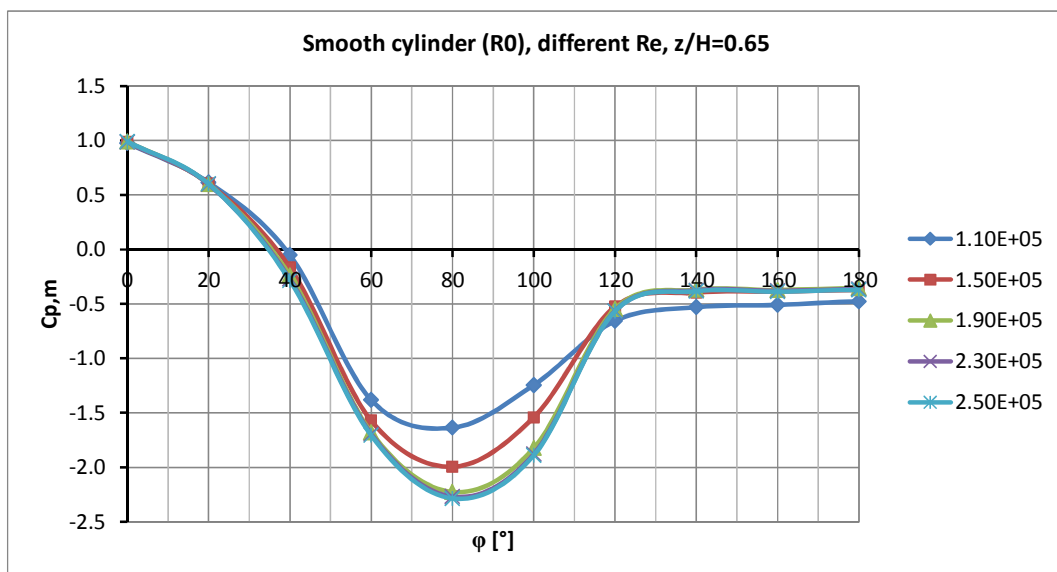


Figure 4.35 Mean pressure distribution as a function of Re on the smooth cylinder ($z/H = 0.65$)

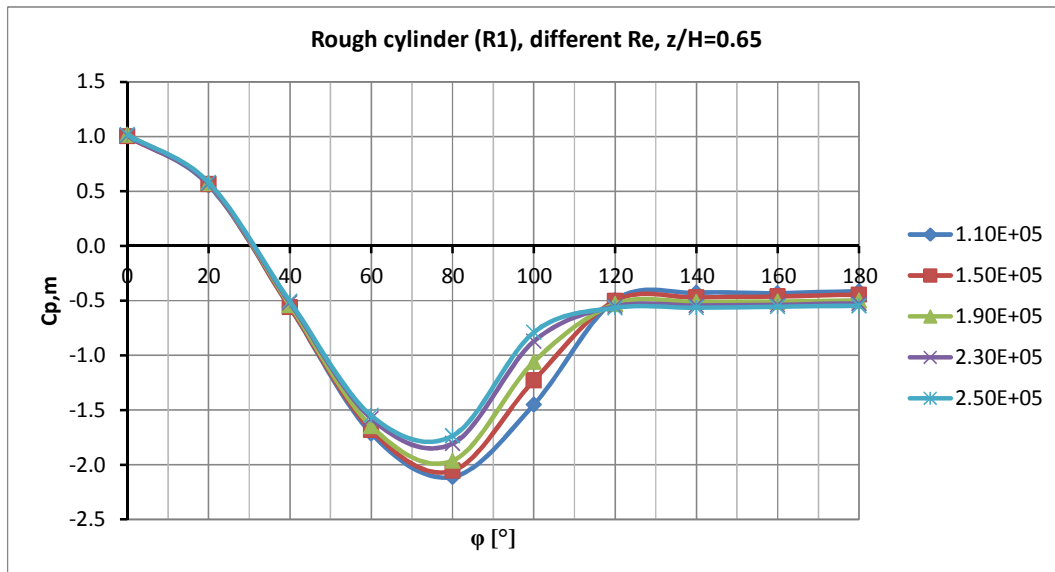


Figure 4.36 Mean pressure distribution as a function of Re on the rough cylinder ($z/H = 0.65$)

In time, the position of the separation point is not stationary, but it fluctuates around the average position, in full-scale as well as in the wind tunnel. The function of the ribs should not be to force the separation at precise locations, but to promote turbulent transition of the boundary layer. A turbulent boundary layer is able to overcome larger adverse pressure gradients and therefore separation is retarded. However, it can be argued whether such oscillations of separation are forced or prevented by the presence of the ribs on the wind tunnel model. Figure 4.37 clarifies that with small surface roughness (e.g. R1) the position of separation is not particularly fixed by the presence (and the specific distribution) of the ribs. The figure highlights the spatial oscillation of the separation point in a short time window. The roughness conditions R4 and R5 resulted, from this point of view, more invasive. In fact, it is not recommended to force the Reynolds regime by using high surface roughness. Ribeiro (1991) wrote: “the larger the relative roughness, the lower the Reynolds number with which the ultra-critical regime is established, but the greater the differences observed in this regime, between the parameters measured on the rough circular cylinder and those observed on smooth circular cylinders”. For this reason, the surface roughnesses R4 and R5 are discarded for further studies on the tower.

The Strouhal number decreases on the rough cylinder (R1) from 0.22 to 0.20 as the transcritical conditions are approached (Figure 4.38) and the peak becomes narrower. Such a decrease in the Strouhal number is related to the upstream movement of the separation point. The lowest S_t on the rough cylinder (R1) at the highest Re (2.5×10^5) is associated to a wider wake, as shown in Figure 4.36. This is consistent with Roshko’s concept of universal Strouhal number, which is related not to the cylinder dimension but to the width of the wake (Roshko, 1955).

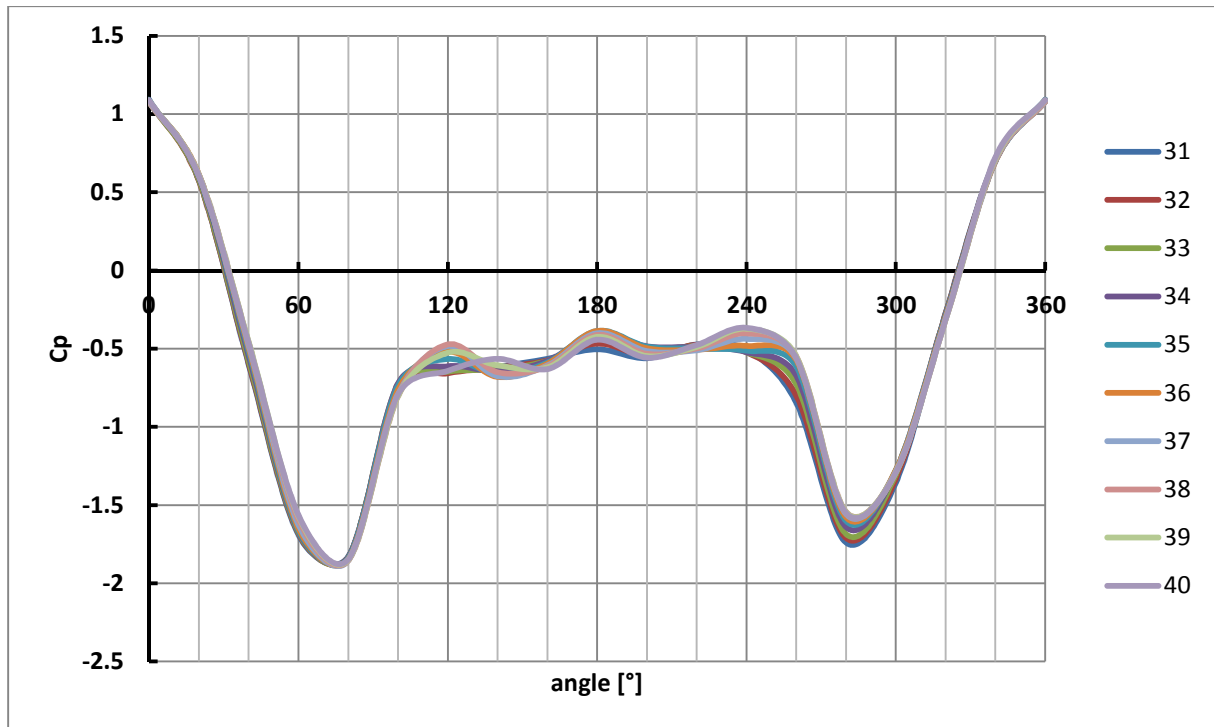


Figure 4.37 Momentary pressure distribution ($z/H = 0.65$, T1-R1, time steps 2897:2906)

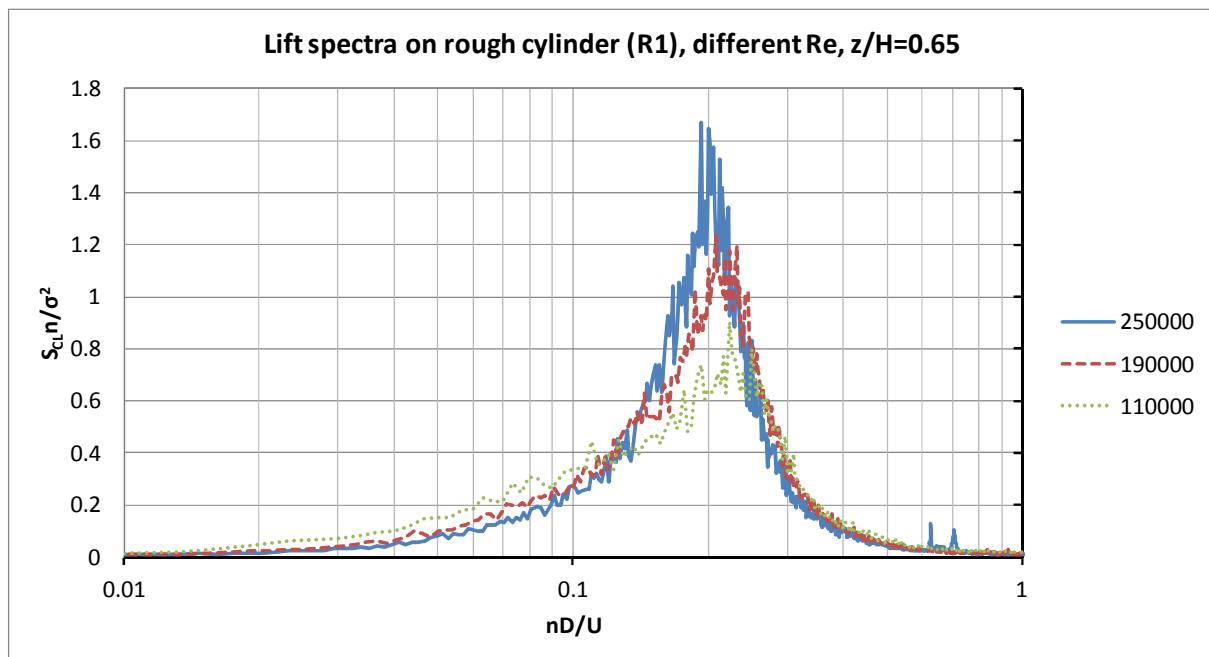


Figure 4.38 Spectra of the lift coefficient vs n [Hz] on the rough cylinder as a function of Re

The skewness of the spectra at $z/H=0.65$ in Figure 4.38, which is more evident at the lowest Re (green curve) but still present at the highest Re , is due to fluctuations produced at low frequencies by tip-associated-vortices. They are free-end effects, as mentioned in Chapter 3 and better investigated in Chapter 5.

So far, the discussion has been focused on the behaviour at middle height.

Figure 4.39 and Figure 4.40 describe the spanwise variation of the mean drag coefficient and of the pressure recovery at $Re = 2.5 \cdot 10^5$. The tip effect is influenced by the surface roughness, because the rougher is the cylinder, the lower is the wake pressure (Figure 4.33). This enhances the flow over the tip of the body. For the same reason, the tip effect on the smooth cylinder is weaker: the smooth cylinder at $Re = 2.5 \cdot 10^5$ is in supercritical conditions, characterized by minimum drag (horizontal plateau) due to small wake suction and very high pressure recovery due to large suction at the flanges. Moreover, in uniform flow (black curve) the tip effect is weaker than in boundary layer flow. It is in contradiction with Gould's conclusion (Gould et al., 1968) that the free-end effect is independent on the type of boundary layer. It is confirmed, instead, that the tip effect produces an increase in the lift fluctuations at about one diameter from the top, probably due to tip vortices, while the spanwise variation of drag fluctuations are less pronounced.

Another important feature in Figure 4.39 and Figure 4.40 is the ground effect, which extends up to $z/H = 0.5$. It is not only confined to the very low region. The higher drag at the base of the tower is probably enhanced by the presence of a boundary layer and thus vertical pressure gradients, as mentioned in Chapter 3. Unfortunately there are not so many measurements at low levels in uniform flow (T3). In this case, a significant variation of $C_{D,m}$ would not be expected. In the presence of atmospheric boundary layer, the ESDU Data Items (ESDU 81017) confirm the existence of higher wake suction and lower pressure at the flanges. The high wake suction is responsible for an increase in drag. The even larger lateral suction produces the increase in pressure recovery as $z \rightarrow 0$. In fact, the correction factor proposed by the ESDU Data Items to account for the atmospheric boundary layer profile (ESDU 81017, figure 5) shows the same trend as the red curve in Figure 4.39. A similar behaviour of the drag curve at low levels is confirmed in literature e.g. by Garg's results (1995) at sub-critical Re , but a systematic study does not exist. The blue curve in Figure 4.39 (smooth cylinder) would suggest an even higher three-dimensionality of the phenomenon. However, there are not measurements in the lower half to confirm it.

The choice of an appropriate surface roughness for the wind tunnel tests, in view of the evaluation of design wind loads, depends on the full-scale condition which one would like to achieve. For solar towers, the target full-scale condition is given by a smooth circular cylinder in transcritical Re . Codified data for smooth and rough surfaces at transcritical Re are available in the VGB guideline (2010). Further full-scale data on chimneys and TV towers are collected in (Niemann&Schröder, 1981).

Relying on the recommendation of the VGB guideline, the target value of the drag coefficient for a smooth surface is in the range 0.46-0.49. The value of the minimum lateral suction (1.5-1.6 for curves K1.5 and K1.6, respectively) should not be considered alone, rather, the difference $C_{p,b} - C_{p,\min}$ is a much more significant parameter, since the base pressure depends on slenderness while the pressure recovery is not so influenced by the aspect ratio. Therefore, referring to cooling towers, for solar towers it should be expected $C_{p,b} - C_{p,\min}$ in the range 1.0-1.1.

On the basis of these recommendations, three different alternatives in terms of rib height and rib distance seem to be equivalent. The highest surface roughness (R4-R5) is discarded, as previously said. By choosing an appropriate value for the wind tunnel velocity, R1, R2 and R3 may be used. Remarkable is also the similarity between R2 and R3 for the whole range of Re . In this work, in view of the design wind loads, the condition R1 at 1400 rpm ($Re = 2.5 \cdot 10^5$) is selected and it will be used in the next chapters.

The pressure results of the experiments, shown in terms of $C_{p,\min}$, $C_{p,h} - C_{p,\min}$ and $C_{p,h}$, are compared with literature (Figure 4.41). Wind tunnel tests in literature at transcritical Re on smooth circular cylinders, providing pressure distributions and not only force measurements, are rare. An investigation is contributed by Gould et al. (1968), who measured pressures on smooth cylinders having different aspect ratio in a pressurized wind tunnel ($Re = 2.7-5.4 \cdot 10^6$). This paper is used here as reference, also in order to prove the effectiveness of surface roughness in the experiments. However, Gould's experiments are in uniform flow and this should explain the departure of results at low levels, as previously mentioned.

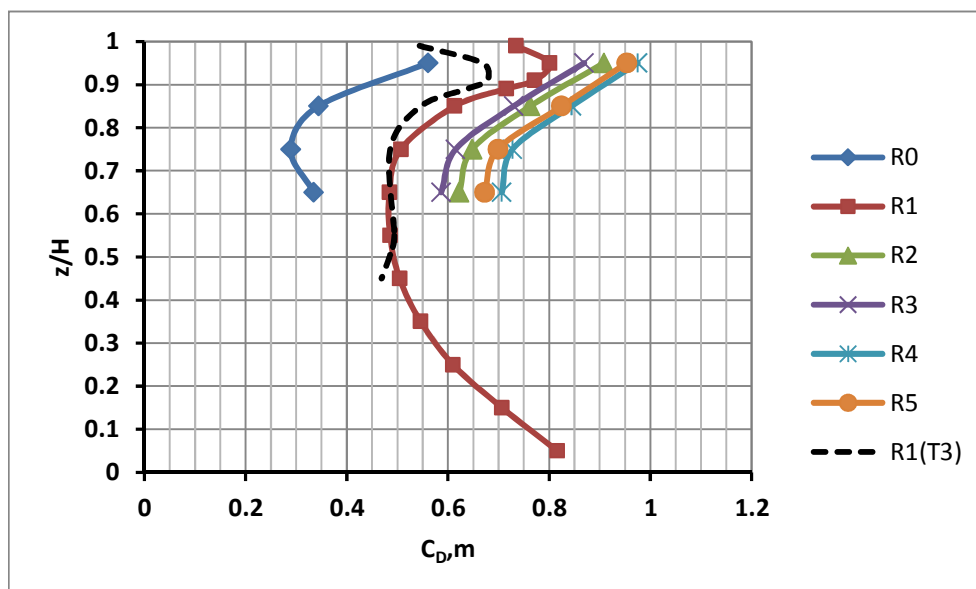


Figure 4.39 Mean drag coefficient along the height on the smooth cylinder and for different roughness conditions at $U_H \approx 25$ m/s, $Re = 2.5 \cdot 10^5$ (R0-R5, T1 unless differently specified)

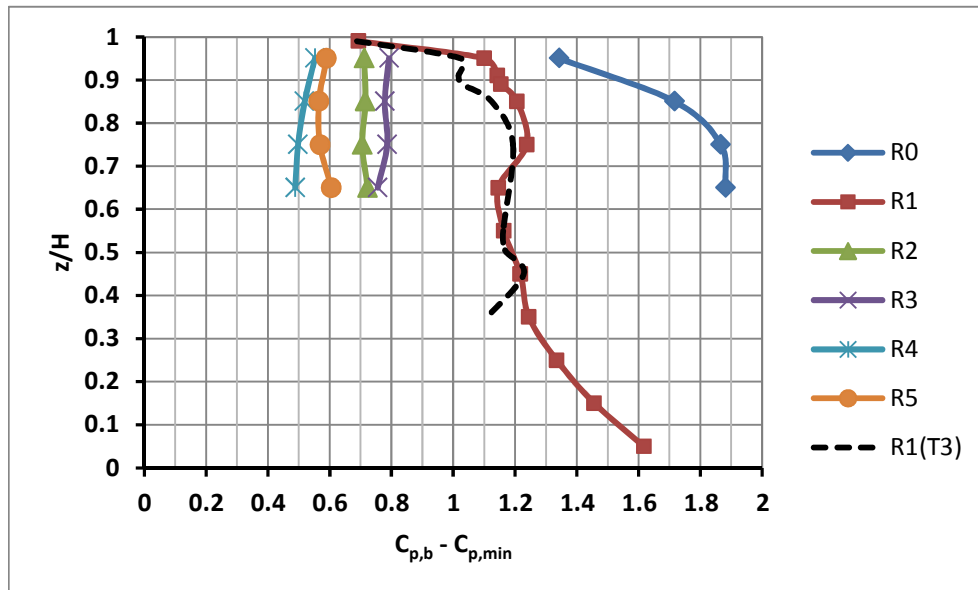


Figure 4.40 Pressure recovery along the height on the smooth cylinder and for different roughness conditions at $U_H \approx 25$ m/s, $Re = 2.5 \cdot 10^5$ (R0-R5, T1 unless differently specified)

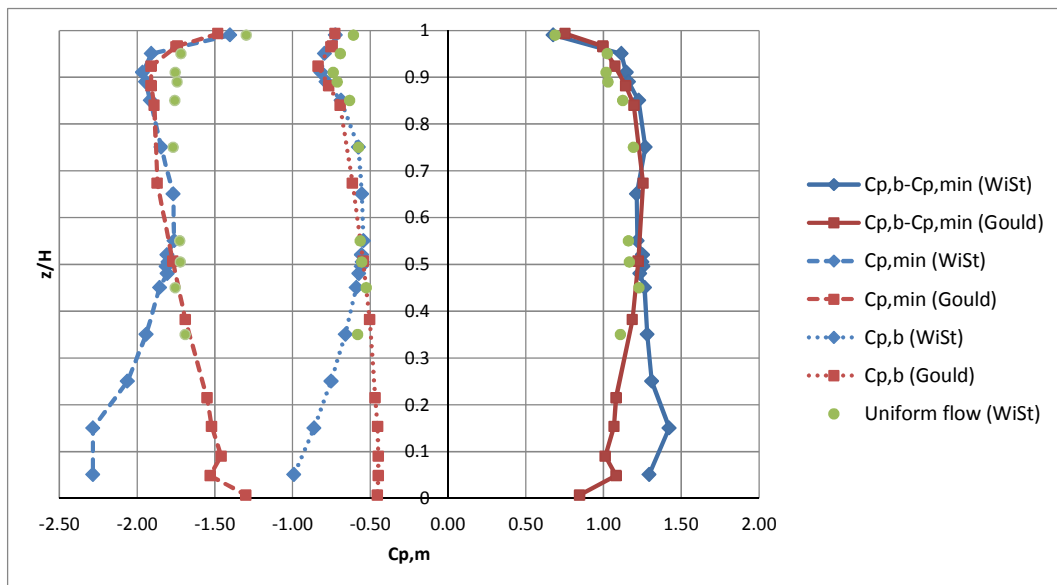


Figure 4.41 Mean pressure coefficients ($C_{p,min}$, $C_{p,b} - C_{p,min}$, $C_{p,b}$): red = results by Gould et al., 1968 ($H/D = 6$, $Re = 5.4 \cdot 10^6$, uniform flow); blue = WiSt (R1-T1). Green = WiSt (R1-T3, i.e. uniform flow)